Inorganic Chemistry

pubs.acs.org/IC

Article

Brønsted Acids as Direct C−H Bond Activators in Conjunction with High-Valent Metal−Oxo Catalysts: Revisiting Metal-Oxo Centered Mechanisms

Neethinathan Johnee Britto,* Asmita Sen, and Gopalan Rajaraman*

Cite This: *Inorg. Chem.* 2025, 64, 5944−5959

Read Online

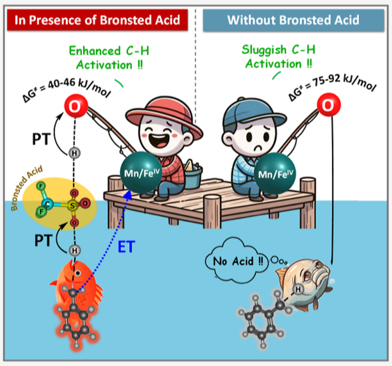

ABSTRACT: High-valent metal-oxo species are ubiquitous in chemistry due to their versatile catalytic reactions and their widespread presence in metalloenzymes. Among the metal-oxo species, $Fe^{IV} = O$ and $Mn^{IV} = O$ species are the most widely studied, and several biomimic models of such species have been created over the years. While various factors such as spin state, ligand design, and redox potential influence the reactivity of these species, a dramatic enhancement of reactivity by *a* factor of 10^2 to 10^8 upon the addition of Lewis (LA) and Brønsted acids (BA) stands out as a striking phenomenon, whose underlying mechanism remains largely unexplored. In this work, we explored the mechanism of BA-promoted C−H activation using $[(N4Py)Mn^{IV}(O)]^{2+}$ (**1**) and $[(N4Py)Fe^{IV}(O)]^{2+}$ (**2**) species to arrive at a generic mechanism for these catalytic transformations. We have explored three possible mechanistic routes: (i) a mechanism of C−H activation followed by −OH rebound without the BA (triflic acid) for the toluene hydroxylation reaction, (ii) a mechanism where triflic acid is a spectator, and (iii) a mechanism where triflic acid directly participates in both electron transfer/proton transfer and C−H bond activation steps. Our calculations reveal that when BAs are added, it is no longer the metal-oxo species that activates the C−H bond (as known conventionally), rather it is the BA that directly performs the C−H activation through an unprecedented mechanistic route. The direct involvement of triflic acid was found to lower the C−H bond activation barrier by approximately 20−30 kJ/mol compared to when it is absent. This reduction is attributed to the triflate anion performing direct C−H bond activation from the toluene radical cation, rather than the conventionally assumed metal-oxo moiety. Among many factors, the formation of ion-pair and the consequent electronic changes incurred, and large localized electric field effect around the S−O bond of the triflic acid was found to be the driving force for the calculated lower barrier height. The theoretical findings corroborate experimental observations, providing the first comprehensive explanation for the enhanced reactivity in the presence of LA/BA acids. These findings have direct implications for enzymatic systems such as the oxygen-evolving complex and open an uncharted path in the catalytic design.

1. INTRODUCTION

Various factors such as the oxidation state and spin state of the metal ion, solvation environment, ligand architecture, axial substitution, and other reaction conditions like temperature have been well established to influence the efficiency of biomimetic high-valent metal−oxo species toward C−H/O−H activation.[1−8] Additionally, in recent years, cofactors such as Lewis acids (LAs) and Bronsted acids (BAs) have been proven to play a crucial role in controlling the electron transfer (ET)/proton transfer (PT) processes and enhancing the catalytic efficiency of the metal−oxo complexes toward different redox reactions. This idea is an inspiration drawn from the oxygen-evolving complex (OEC) in photosystem II (PSII), which contains Ca^{2+} as an essential cofactor alongside the four manganese-oxo centers (Mn_4Ca), illustrating the importance of cofactors in natural systems.[9,10] Despite significant experimental studies with most of the reports revealing improved performance when LA/BA is added, their role and function in the catalytic cycle remain elusive.[11−24] In order to understand the role of cofactors in nature, several biomimetic studies have emerged demonstrating that binding of redox inactive LAs such as Zn^{2+}, Sc^{3+}, Ce^{4+}, Fe^{3+}, and Ca^{2+} ions to the metal−oxo moiety improved the catalytic rate and selectivity.[25−44] Besides LAs, the addition of BAs such as sulfuric acid (H_2SO_4), perchloric acid ($HClO_4$), and triflic acid (HOTf) have been reported to remarkably enhance the reactivity of metal−oxo complexes toward both oxygen atom transfer (OAT) and hydrogen atom transfer (HAT) reactions.[31−37] These reactions fall under the well-studied proton-coupled electron transfer (PCET) category.[38−41] Experimental observations suggest that binding of LAs or BAs to the metal−oxo unit increases the reduction

Received: November 19, 2024
Revised: February 19, 2025
Accepted: February 24, 2025
Published: March 18, 2025

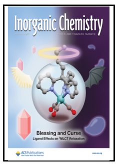

https://doi.org/10.1021/acs.inorgchem.4c04948
Inorg. Chem. 2025, 64, 5944−5959

Scheme 1. Comparison between (a) Conventionally Known Toluene Hydroxylation Mechanism and (b) Proposed Bronsted Acid-Mediated Mechanism

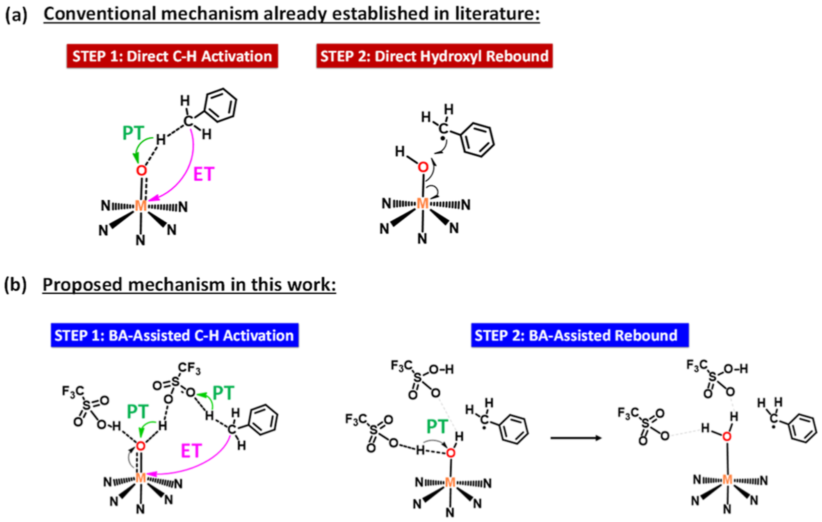

potential of the complexes, which in turn is expected to enhance the efficiency.[11,34,38,40,42] Nevertheless, the substantial increase in reaction rates, ranging from 10^2- to 10^8-fold, along with the observed changes in selectivity of metal−oxo complexes upon forming adducts with LAs and BAs, suggests a possible alteration in the reaction mechanism that is often challenging to be established using experimental studies.[11,19,20,25,27,31,34,35] While the enhanced reactivity is often attributed to factors such as redox potential or activation energy, other mechanistic and electronic contributions, including the influence of the localized electric field (LEF), remain inadequately studied. Acids can protonate the metal-oxo unit, thereby enhancing the electrophilicity of the active site, modulate the LEF, induce charge polarization (ion-pair effects), and stabilize high-energy transition states.[43]

Theoretical studies, especially those employing density functional theory (DFT), have proven instrumental in providing mechanistic insights and guiding the development of more efficient catalysts and this has been demonstrated in the OAT reactions with various metal oxo species.[37,44,45] As BAs are known to undergo reactions via the PCET mechanism, understanding the HAT reaction with metal−oxo species is crucial for uncovering their role in the catalytic cycle. Despite significant experimental studies on this reaction have been reported, the role of BAs and the underlying mechanism have not yet been thoroughly investigated. In this regard, we have selected two complexes, $[(\mathrm{N4Py})\mathrm{Mn}^{\mathrm{IV}}(\mathrm{O})]^{2+}$ (**1**) and $[(\mathrm{N4Py})\mathrm{Fe}^{\mathrm{IV}}(\mathrm{O})]^{2+}$ (**2**) (N4Py = *N*,*N*-bis(2-pyridylmethyl)-*N*-bis(2-pyridyl)methylamine) as representative nonheme metal−oxo models to unravel the mechanism and role of BAs in promoting HAT reactions.[5,46−51] In the presence of HOTf, the metal-oxo groups of 1 and 2 were found to form an adduct with two HOTf molecules, denoted as $[(\mathrm{N4Py})\mathrm{Mn}^{\mathrm{IV}}(\mathrm{O})]^{2+}-(\mathrm{HOTf})_2$ (**1-(HOTf)$_2$**) and $[(\mathrm{N4Py})\mathrm{Fe}^{\mathrm{IV}}(\mathrm{O})]^{2+}-(\mathrm{HOTf})_2$ (**2-(HOTf)$_2$**), and a significant enhancement in the rate of hydroxylation of toluene derivatives up to ∼10^4 orders was observed, especially when hexamethylbenzene (HMB) is the substrate.[25,52] Furthermore, experimental studies reveal that when the hydrogen atoms of the substrate are replaced with deuterium, large deuterium kinetic isotopic effect (KIE) values were noted in the absence of HOTf, indicating that the rate-determining step (rds) of substrate oxidation operates via a conventional HAT mechanism (see Scheme 1a for the mechanism).[26,33] However, in the presence of HOTf, the deuterium KIE was found to be markedly decreased to 1.0 [with an increasing HOTf concentration at 293 K for **1-(HOTf)$_2$** and 298 K for **2-(HOTf)$_2$**], suggesting a possible shift in the rate-determining mechanism. This raises the question of whether the switchover in the mechanism is triggered by the active participation of HOTf in the rate-determining C−H activation step by protonating the metal−oxo moiety. In this case, as portrayed in Scheme 1b, the deprotonated anion part of BA may eventually abstract the proton from the substrate (BA-assisted C−H activation), competing with the conventional mechanism (direct C−H activation, Scheme 1a) where hydrogen/proton will be abstracted directly by the metal−oxo moiety. Also, in the subsequent rebound step, before the hydroxyl moiety is transferred to the substrate radical, another BA may again protonate the metal−hydroxyl moiety to produce a metal−$\mathrm{OH_2}$ species (see Scheme 1b). This also rationalizes the reason for the presence of two HOTf molecules in the vicinity of the catalyst.

The formation of metal−$\mathrm{OH_2}$ species can impact the rebound step and alter the product selectivity.[53,54] Considering these ambiguities and the importance of comprehending the effect of protons on metal−oxo complexes in synthetic and biologically important redox reactions, we have undertaken an extensive computational investigation to provide molecular-level insights into the mechanism of BA-promoted HAT reactions. Specifically, we aim to answer the following open questions that are not only relevant to LA/BA-based catalysis but also have relevance to the mechanism of action in the OEC: (1) does BA participate directly in the C−H activation by abstracting a proton from the substrate (as proposed in Scheme 1b)? (2) Is the −OH rebound step altered in the presence of HOTf? (3) What is the reason for the drastic variation in the KIE observed in the presence and absence of HOTf in the toluene hydroxylation reaction? (4) What is the electronic origin of the remarkable acceleration in rate in the presence of HOTf?

2. COMPUTATIONAL DETAILS

The Gaussian 16 suite was used to carry out all DFT calculations.[55] Given the earlier precedents of UB3LYP[56−58] functional was successfully proven to be capable of predicting reliable energetics, geometry, and spin state ladder for high valent metal−oxo chemistry,[59−61] this study also employs this functional throughout our study. Notably, the benchmarking studies by de Visser, Siegbahn, and Li groups[62−64] further affirm the reliability of this functional. Grimme's D3 version of correction was employed to account for the dispersion effect.[65,66] The nonmetal atoms were described by 6-31G(d,p)[67] basis set, and the metal centers were described with Stuttgart/Dresden's[68] effective core potential. Additionally, to verify the suitability of the chosen methodology for the selected catalysts, we computed the absorption spectra for **1-(HOTf)$_2$** using the TDDFT method to compare it with the experimental data. Our calculations predict a band at 562 nm that corresponds to the d−d transition between the Mn(d_{xz})-O(π^*) to Mn($d_{x^2-y^2}$) orbital (see Figure S1 in ESI), and this matches well with the experimental value of 550 nm offering confidence in the chosen methodology.[33] The free energy correction terms were obtained from the harmonic frequency calculations carried out on the optimized structures at 298.15 K. The transition states were characterized as first-order saddle points using the frequency analysis, and all the reactants, products, and intermediates were found to be true minima. Single-point calculations with triple-ζ quality Def2-TZVPP[69,70] basis set on all atoms incorporating solvation effects using the polarizable continuum model (PCM; acetonitrile)[71] were carried out to obtain reliable energetics as established earlier.[72] To assess if the solvation model artificially favors protonation of the metal-oxo species (see below), we performed additional calculations without the PCM model. These calculations show that the protonated species are exothermic in the gas phase [−53.3 kJ/mol and −59.1 kJ/mol for ^{4}**1-(HOTf)$_2$** and ^{4}**2-(HOTf)$_2$**, respectively; see below] and slightly endothermic in the solvent phase, indicating that PCM solvation does not affect the protonation state. The ORCA 5.0[73] suite was also used to perform the complete active space self-consistent field (CASSCF)[74] calculations with a CAS(9,8) active space on complex **1-(HOTf)$_2$** to assess and analyze the nature of the ground state with respect to the one obtained from the DFT calculations. The eight orbitals in the active space correspond to the nb, π_x^*, π_y^*, σ_{eq}^*, and σ_z^* orbitals of Mn and three oxo orbitals (p_π/p_σ). For transition-state structures, the C−H bonding (σ_{CH}) orbital was included in the CAS, excluding one of the oxygen orbitals. The DKH-Def2-SVP basis set was used for all atoms except for metals, which were treated with DKH-Def2-TZVP. Further additional CASSCF calculations were performed for the Mn^{IV}=O catalyst for both the reactant and the transition state to elucidate the excited state reactivity that arises from the excited quartet states.[75−77] This has been witnessed earlier, particularly in Mn-oxo chemistry, and termed as identical spin-multistate reactivity (ISMR).[78] Using this protocol, we have identified other quartet transition states within DFT calculations.

The Chemcraft program was used to plot the optimized geometries, spin densities, and Frontier molecular orbitals (FMOs). The natural bond orbital (NBO)[79] analysis and wave function for quantum theory of atoms (QTAIM) analysis were generated at the same level of theory used for geometry optimization. AIM2000[80] program was employed to extract all topological properties. The energy decomposition analysis (EDA) was carried out using the Multiwfn program.[81] The Titan[82] code was utilized to simulate the LEF, while the oriented external electric field was applied to the optimization process using the Gaussian 16 program.

3. RESULTS

Experimental studies indicate that the addition of HOTf results in two molecules of HOTf being bound to the metal−oxo species via a strong hydrogen bonding interaction in **1-(HOTf)$_2$**.[52] Similarly, in the case of complex **2-(HOTf)$_2$** as well, experimental analysis of one-electron reduction potential dependence on HOTf suggested to the possibility of binding of two HOTf to the Fe^{IV}=O group.[26] Therefore, based on earlier report,[72] and experimental evidence, **1-(HOTf)$_2$** and **2-(HOTf)$_2$** are considered as the starting point for the mechanistic discussion (see Figure 1). From the optimized geometries, it is noticeable that the HOTf molecules are bound to the metal−oxo species via strong hydrogen bonding interactions ranging between 1.595 and 1.719 Å. As a consequence, metal−oxo bonds are elongated from 1.640 Å in ^{4}**1** to 1.672 Å in ^{4}**1-(HOTf)$_2$** and from 1.618 Å in ^{3}**2** to 1.638 Å in ^{3}**2-(HOTf)$_2$**. In addition, the radical character of the oxyl oxygen atom was found to be diminished and the ionic character of the M−O bond enhanced, as evidenced by the increase in computed natural charges and spin densities [q_O of **−0.416** in ^{4}**1** vs **−0.624** in ^{4}**1-(HOTf)$_2$**; −0.261 in ^{3}**2** vs −0.453 in ^{3}**2-(HOTf)$_2$**; and ∼0.20 decrease in oxyl and *ca* same amount increase in metal]. This is also supported by the NBO analysis of percentage orbital composition of the M−O bond [for ^{4}**1** Mn(**42**.1%; $d_z{}^2$)−O(49.1%; p_z) bond vs ^{4}**1-(HOTf)$_2$** Mn(26.6%; $d_z{}^2$)−O-(73.41%; p_z); ^{4}**2** Fe(49.1%; $d_z{}^2$)−O(50.9%; p_z) bond vs ^{4}**2-(HOTf)$_2$** Fe(23.5%; $d_z{}^2$)−O(76.7%; p_z)]. This decrease in the radical character at the oxyl center and increase in the ionic nature of the metal−oxo bond in ^{4}**1-(HOTf)$_2$** and ^{3}**2-(HOTf)$_2$** renders them favorable for the abstraction of protons rather than the abstraction of a hydrogen atom (HAT). Further CASSCF calculations on ^{4}**1** and ^{4}**1-(HOTf)$_2$** reveal multiple low-lying quartet states, crucial for the Mn^{IV}=O species, which exhibit multireference characteristics. Shaik and co-workers[48] suggested that these excited states could lower kinetic barriers, a concept supported by experimental evidence, including MCD spectra,[83]

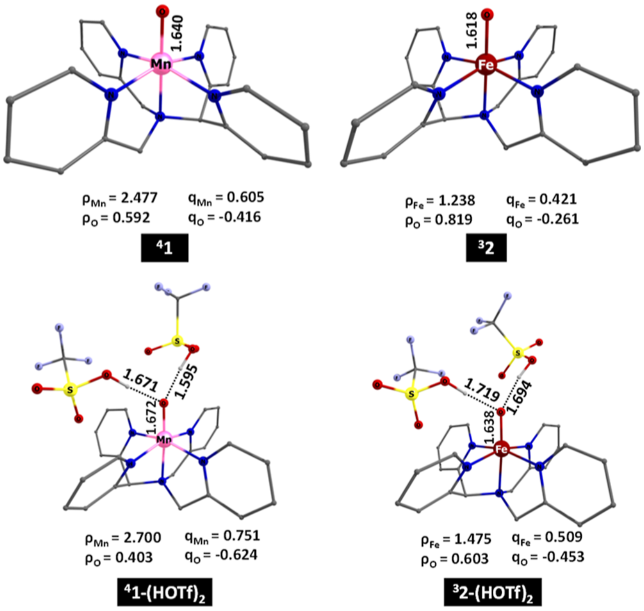

Figure 1. Optimized ground-state geometries of **1**, **2**, **1-(HOTf)$_2$** and **2-(HOTf)$_2$** with pertinent bond lengths (in Å) along with spin densities on notable atoms.

showing the presence of such states and opening new reactivity channels. Even for five-coordinate Mn-oxo/oxo/hydroxo species, a similar reactivity was observed. Our analysis identifies two low-lying quartet states for ^{4}**1** (^{4}**B$_1$-1** and ^{4}**E$_1$-1**), with a 1.2 kJ/mol energy difference, which increases to 25.1 kJ/mol upon adding HOTf.

This change is also reflected in the computed activation energies and choice of the mechanistic pathway discussed below. As toluene hydroxylation takes place in two steps: (i) C−H activation and (ii) hydroxyl rebound processes, we have explored three different mechanistic pathways for each of these steps, as depicted in Figure 2. The first pathway explores the conventional mechanism of direct toluene hydroxylation catalyzed by **1** and **2** in the absence of HOTf. In the second pathway, the mechanism of the entire toluene hydroxylation catalyzed by **1-(HOTf)$_2$** and **2-(HOTf)$_2$** is evaluated, where the HOTf molecules bound to the metal−oxo unit are assumed to be a spectator throughout the hydroxylation reaction. In the third pathway, HOTf is assumed to actively participate in both C−H activation as well as in rebound steps.

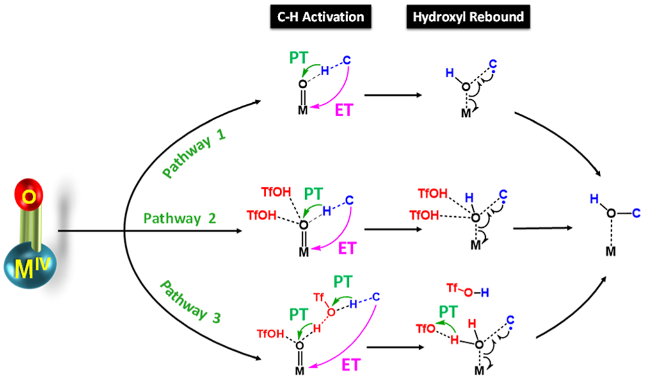

Figure 2. Three possible mechanistic pathways explored in the present work to understand the role of BAs in toluene hydroxylation catalyzed by high-valent metal−oxo complexes.

3.1. Mechanism of C−H Activation.

3.1.1. Conventional Direct C−H Activation by 1 and 2 without HOTf (Pathway 1).

To comprehend the influence of HOTf on the toluene hydroxylation mechanism, the entire mechanism was initially studied in the absence of HOTf molecules (see Figure 3a for the mechanism), and the corresponding computed free energy profiles for direct hydroxylation of toluene catalyzed by 1 and 2 are displayed in Figure 3b,c. All the intermediates and transition states involved in the reaction were optimized in three possible spin states: S = 1/2, S = 3/2, and S = 5/2 for 1. The S = 5/2 arises for an electromeric form of Mn^{IV}−oxo complex, i.e., Mn^{III}−O$^\bullet$ where ferromagnetic coupling between Mn^{III} and the O$^\bullet$ is assumed. It is important to note that antiferromagnetic coupling in the Mn^{III}−O$^\bullet$ motif would result in S = 3/2 state when the metal−ligand bond lengths are relatively longer.[84] In the case of 2 as well, the three low-lying spin multiplicities (S = 0, 1, and 2) were considered for the mechanistic investigation. In accordance with earlier experimental and computational reports, our calculations predict the S = 3/2 spin state to be the ground state for 1 and the S = 1 state for complex **2**.[84,85] The free energies for the formation of reactant complexes are calculated to be endergonic by 26.6 and 25.2 kJ/mol for both ^{4}**1-RC$_{Mn}$** and ^{3}**2-RC$_{Fe}$**, respectively. In the ensuing step, direct C−H activation takes place, where one of the hydrogens from the methyl group of toluene is abstracted by the metal−oxo moiety, while one

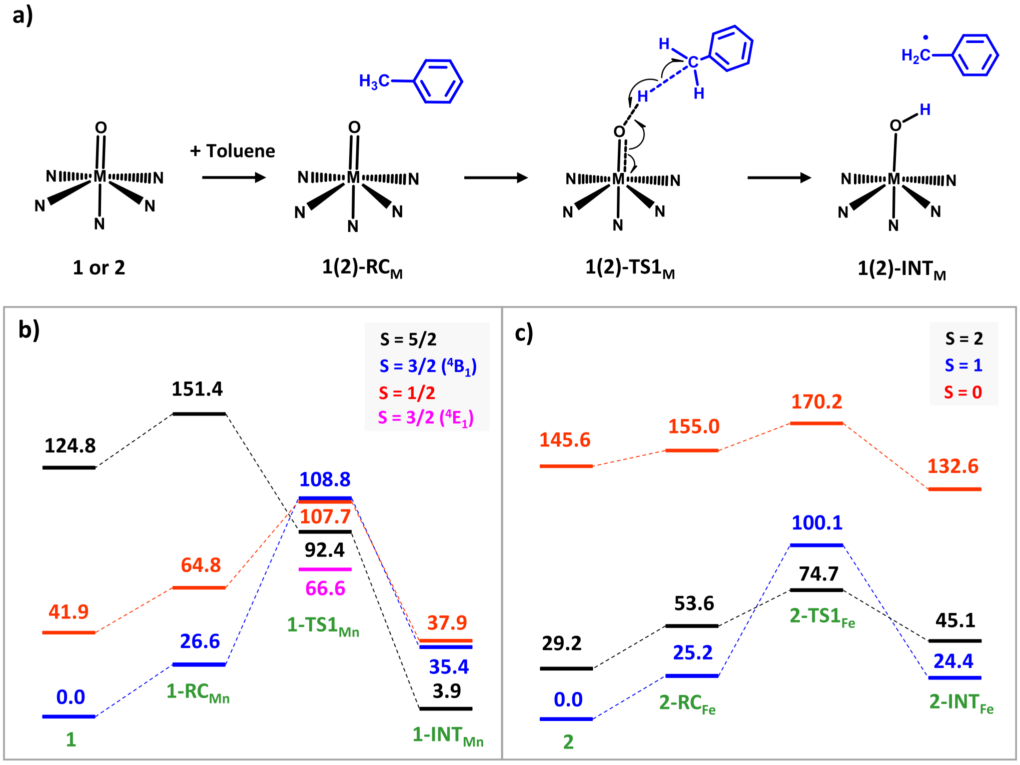

Figure 3. (a) Conventional mechanism of direct C−H activation of toluene without HOTf, and (b) corresponding computed free energy profile (in kJ/mol) for the same catalyzed by **1** and (c) **2**.

electron transfer from toluene to the metal center occurs simultaneously via transition state **1(2)-TS1$_M$**.

As discussed above, the CASSCF results highlight the importance of analyzing other excited quartet states for the Mn^{IV}═O species to determine if ISMR-type reactivity is accessible.[78] As the excited state ($^4E_1$) transition state for the S = 3/2 spin surface is also shown to participate in the reaction, we have computed this particular transition state as well (denoted as **^{4}E$_1$-1-TS1$_{Mn}$**). The minimum activation energy estimated for this step is 66.6 kJ/mol for **^{4}E$_1$-1-TS1$_{Mn}$** and 74.7 kJ/mol for **^{5}2-TS1$_{Fe}$** while the corresponding transition state of ground spin states was found to be higher in energy. This demands a two-state reactivity scenario with a minimum energy crossing point (MECP) from triplet to quintet state in the case of 2.[86] We have computed the MECP for the triplet to quintet transition for **2**, and this is estimated to be 69.4 kJ/mol, which is nearly equal to the estimated kinetic barrier, suggesting a possible switch from the triplet to quintet state to facilitate the reactivity. The optimized geometries and the spin density plots of the transition state structures **^{4}E$_1$-1-TS1$_{Mn}$** and **^{5}2-TS1$_{Fe}$** are displayed in Figure 4. The bond lengths of Mn−O and Fe−O bonds are found to be 1.733 and 1.669 Å for **^{4}E$_1$-1-TS1$_{Mn}$** and **^{5}2-TS1$_{Fe}$**, respectively. The ∠Mn−O−H bond angle in **^{4}E$_1$-1-TS1$_{Mn}$** is estimated to be 117.9°, indicating that the C−H bond is activated via a π-channel while a σ-pathway (158.4°) is operative in **^{5}2-TS1$_{Fe}$**. A relatively shorter O−H bond length of 1.303 Å is noted in **^{4}E$_1$-1-TS1$_{Mn}$** compared to 1.557 Å in ^{5}2-TS1$_{Fe}$, as C−H activation through π-channel necessitates the overlap of $\pi_{(d_{xy,yz}+P_{x,y,z})}$ orbital of Mn−O bond with $\sigma_{(P_{x,y})}$ orbital of C−H bond. Analysis of their spin density plot (Figure S2) shows that nearly 57% of the spin-up electron has been transferred from toluene to metal-oxo orbital $\sigma_{(d_{x2-y2}+p_z)}$ in **^{4}E$_1$-1-TS1$_{Mn}$** as the spin density on the Mn center increased to 3.795. In contrast to this, at **^{5}2-TS1$_{Fe}$**, no electron transfer from the substrate to the catalyst is witnessed. In the next step, the formation of **2-INT$_{Fe}$** is assumed, and here, the triplet state is found to be the ground state, suggesting an MECP after the formation of the transition state. At this ^{3}2-INT$_{Fe}$ intermediate, electron transfer from the substrate to the catalyst occurs with 77.8% of β-electrons from the substrate transferred to the oxygen moiety (Figure S3). The formation of the intermediate with metal−hydroxyl species and a benzyl radical is estimated to be slightly endergonic for **^{3}2-INT$_{Fe}$** (24.4 kJ/mol) compared to **^{6}1-INT$_{Mn}$** (3.9 kJ/mol).

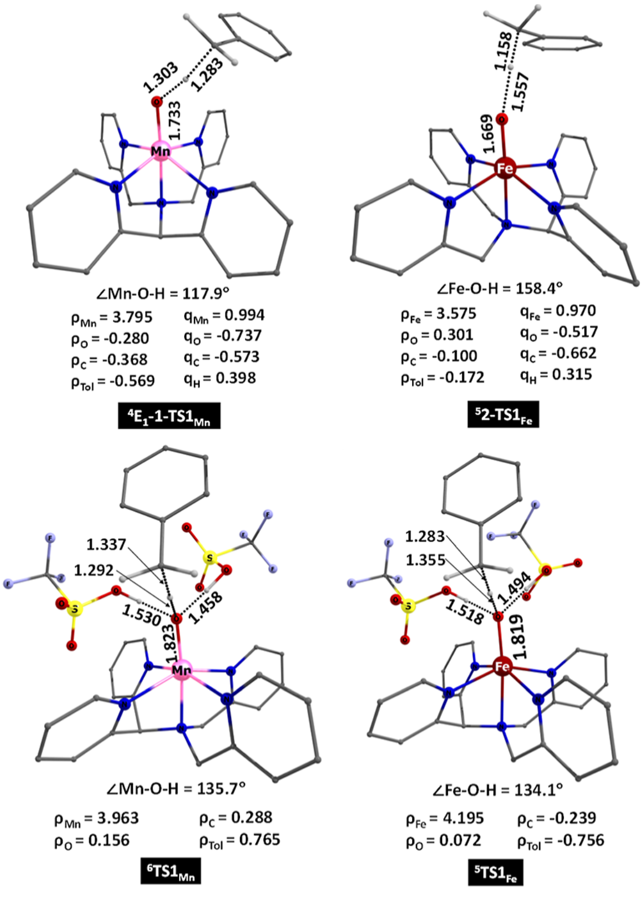

Figure 4. Optimized geometries of **^{4}E$_1$-1-TS1$_{Mn}$**, **^{5}2-TS1$_{Fe}$**, **^{6}TS1$_{Mn}$**, and **^{5}TS1$_{Fe}$**, with their structural parameters (bond lengths in Å and bond angles in °).

*3.1.2. C−H Activation by **1-(HOTf)$_2$** and **2-(HOTf)$_2$** with HOTf as a Spectator (Pathway 2).* In this pathway, C−H activation follows the same mechanism as described earlier but in the presence of HOTf molecules that are explicitly present at the active site. As established earlier, two HOTf molecules are expected to coordinate with the metal−oxo species, and therefore, we have considered this model for the present study (**1-(HOTf)$_2$** and **2-(HOTf)$_2$**). In this pathway, the HOTf molecules are assumed to provide only electronic and steric influences on the reactivity without their direct participation (see Figure 5a). In accordance with the experimental EPR spectrum and ^{1}H NMR results,[33,87] our calculations predict the S = 3/2 spin state to be the ground state for **1-(HOTf)$_2$** with the doublet and sextet geometries lying higher at 82.4 and 161.4 kJ/mol, respectively (see Figure 5b). Additionally, ab initio CASSCF calculations were performed on **1-(HOTf)$_2$**, revealing that the quartet surface is indeed the ground state. In the case of **2-(HOTf)$_2$** (see Figure 5c), our calculations predict S = 1 as the ground state, which is, consistent with available experimental/computational data.[80,81] The **^{1}2-(HOTf)$_2$** and **^{5}2-(HOTf)$_2$** species are higher in energy by 114.6 and 42.0 kJ/mol, respectively, from the ground state. The formations of **^{4}RC$_{Mn}$** and **^{3}RC$_{Fe}$** are estimated to be endergonic by 15.1 and 17.9 kJ/mol, respectively. This is relatively less endergonic compared to the formation free energies of **^{4}1-RC$_{Mn}$** and **^{3}2-RC$_{Fe}$** (26.6 and 25.2 kJ/mol) without the HOTf molecules, indicating that the hydrogen bonding interactions between two HOTf molecules and metal−oxo moiety have stabilized the reactant complex formation energy by around 10 kJ/mol. Once the reactant complex (**RC$_M$**) is formed, the metal−oxo moiety directly abstracts a hydrogen atom from the (sp^3)C−H bond of toluene through **TS1$_M$**. The barrier height is estimated to be 80.6 kJ/mol (53.4 kJ/mol) for **^{6}TS1$_{Mn}$** (**^{5}TS1$_{Fe}$**), while the **^{2}TS1$_{Mn}$** (**^{3}TS1$_{Fe}$**) and **^{4}TS1$_{Mn}$** (**^{1}TS1$_{Fe}$**) transition states are found higher in energy by 28.5 kJ/mol (23.2 kJ/mol) and 43.2 kJ/mol (102.1 kJ/mol), respectively. At this transition state, one-electron transfer from toluene to the metal center is witnessed for both the Mn and Fe species. Similar to the direct C−H activation mechanism (pathway 1), a spin-crossover from triplet to quintet spin surface is needed for the reaction to proceed suggesting the popular TSR reactivity for the Fe^{IV}═O species. For complex **1-(HOTf)$_2$**, however, no such switch is required as during the transition state, as stated earlier, only a switch in the *J* from the antiferromagnetic state $\overset{\uparrow\uparrow\uparrow\uparrow}{Mn^{III}}$—$\overset{\downarrow}{O}$• to the ferromagnetic state $\overset{\uparrow\uparrow\uparrow\uparrow}{Mn^{III}}$—$\overset{\uparrow}{O}$• is required during the course of the reaction. Upon comparing the computed activation free energy required for conventional

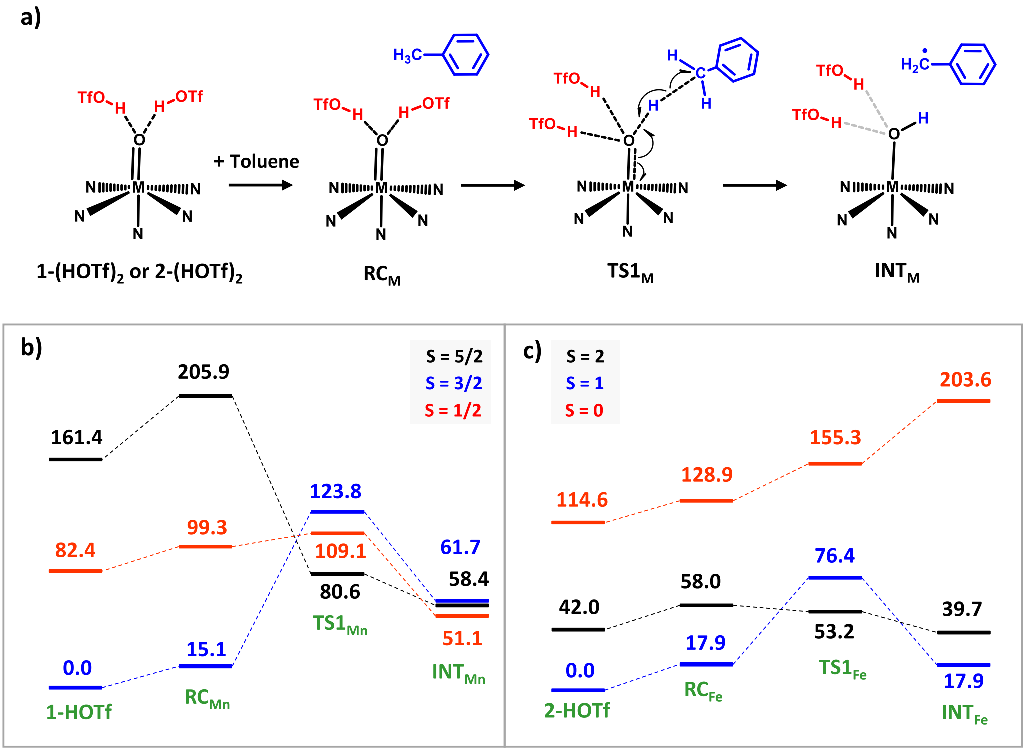

Figure 5. (a) Mechanism of direct C−H activation of toluene with HOTf acting as a spectator, and their corresponding (b) computed free energy profiles (in kJ/mol) for catalysts **1-(HOTf)$_2$** and (c) **2-(HOTf)$_2$**.

Scheme 2. Proposed Mechanism for Bronsted Acid-Mediated C−H Activation of Toluene by High-Valent Metal−Oxo Complexes

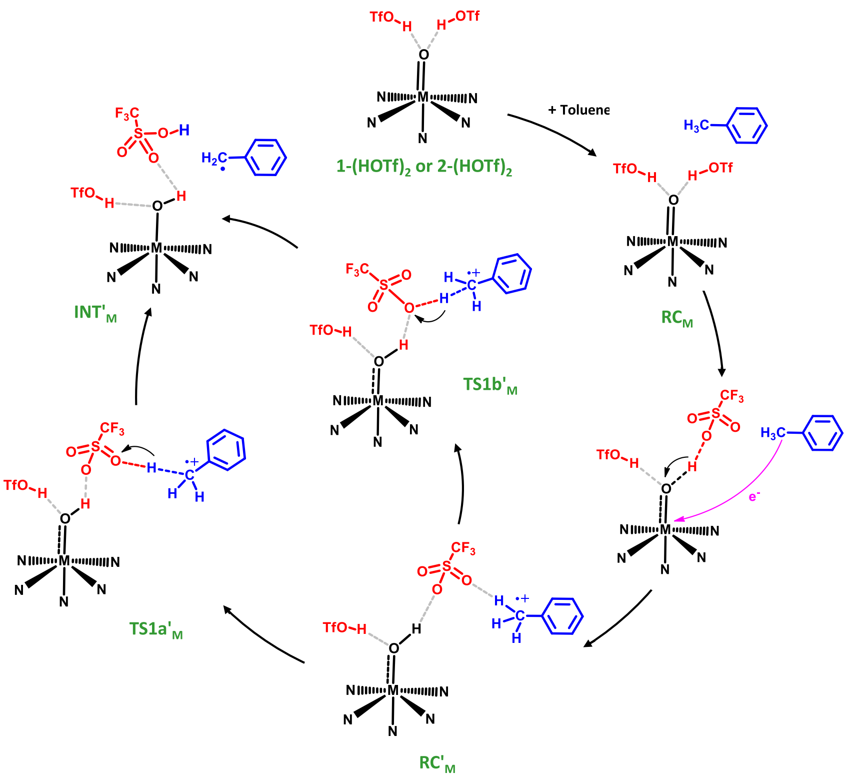

direct C−H activation without HOTf (66.6 kJ/mol for $^{4}E_{I}$-**1**-**TS1**$_{Mn}$ and 74.7 kJ/mol for ^{5}**2**-**TS1**$_{Fe}$), it is evident that the interactions of HOTf molecules with metal−oxo moiety in ^{6}**TS1**$_{Mn}$ and ^{5}**TS1**$_{Fe}$ have increased the activation free energy by 20.0 kJ/mol and decreased the barrier by 21.5 kJ/mol, respectively. The metal−oxo bond lengths are found to be significantly elongated in ^{6}**TS1**$_{Mn}$ and ^{5}**TS1**$_{Fe}$ to 1.823 and 1.819 Å, respectively, compared to the same in $^{4}E_{I}$-**1**-**TS1**$_{Mn}$ and ^{5}**2**-

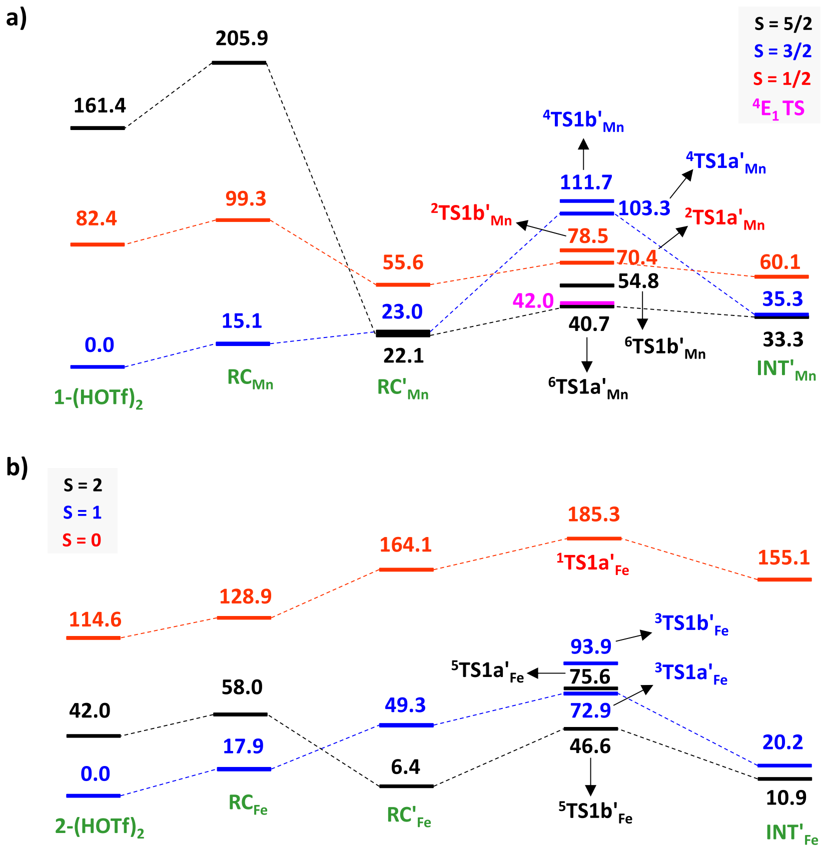

Figure 6. Calculated free energy profiles (in kJ/mol) for HOTf-mediated C−H bond activation catalyzed by (a) **1-(HOTf)$_2$** and (b) **2-(HOTf)$_2$**.

TS1$_{Fe}$ (1.743 and 1.669 Å, respectively; see Figure 4). This is mainly due to steric crowding at the catalytic site by HOTf molecules, making the metal-oxo unit inaccessible to the substrate unless the metal-oxo bonds are significantly elongated, as evidenced in the computed transition state. The ∠Fe−O−H bond angle in ^{5}**TS1$_{Fe}$** is found to be decreased to 134.1° from 158.4° in ^{5}**1-TS1$_{Fe}$**, suggesting a switch in the channel from σ-pathway to π-pathway in the presence of HOTf. The ∠Mn−O−H bond angle in ^{6}**TS1$_{Mn}$**, although it increases to 126.4° from 117.9° in ^{4}**E$_1$-1-TS1$_{Mn}$**, changes are relatively small, and the π-pathway is retained in the presence of HOTf. Furthermore, in contrast to ^{5}**1-TS1$_{Fe}$**, significant spin density (−0.756) is found in toluene in ^{5}**TS1$_{Fe}$**, indicating that an α-electron transfer has been transferred to the catalyst in the transition state (Figure S2). Thus, strong hydrogen bonding interaction with HOTf molecules has led to the elongation of the metal−oxo bond while decreasing the ∠M−O−H bond angles to facilitate a facile ET process, leading to a reduction in the associated kinetic barrier for C−H activation in ^{5}**TS1$_{Fe}$** compared to the mechanism established in the absence of HOTf. The resultant intermediate is found to be relatively more endergonic than the corresponding intermediates without HOTf interaction in the case of Mn catalyst (51.1 kJ/mol for ^{2}**INT$_{Mn}$** vs 3.9 kJ/mol for ^{6}**1-INT$_{Mn}$**), while it is the reverse in the case of Fe catalyst (17.9 kJ/mol for ^{3}**INT$_{Fe}$** vs 24.4 kJ/mol for ^{3}**2-INT$_{Fe}$**), suggesting that intermediate formation in the absence of HOTf is more favorable for Mn catalyst compared to its presence, and vice versa for Fe catalyst, possibly hinting at the dynamic role of HOTf in the reaction mechanism.

*3.1.3. HOTf-Mediated C−H Activation by **1-(HOTf)$_2$** and **2-(HOTf)$_2$** (Pathway 3):* As an alternative to the two pathways discussed above, here we consider the possibility of HOTf molecules directly participating in the C−H activation process (see Scheme 2). According to this mechanism, after the formation of the reactant complex (**RC$_M$**), the metal−oxo moiety that is in hydrogen bonding interaction with the HOTf molecules is expected to abstract a proton from one of the two HOTf molecules to generate another reactant complex (denoted as **RC′$_M$** in Scheme 2). While this is expected to proceed via a transition state, our relaxed scan revealed that its formation is a barrier-less process in all three spin surfaces (see Figure S4 in ESI). From the computed free energy profile for this pathway (shown in Figure 6), it can be seen that this protonation of the metal-oxo unit yields a sextet state as the ground state (^{6}**RC′$_{Mn}$**) with an estimated formation free energy of +7 kJ/mol relative to ^{4}**RC$_{Mn}$**. The ^{4}**RC′$_{Mn}$** and ^{6}**RC′$_{Mn}$** surfaces are close-lying with a very negligible quartet-sextet gap (<1 kJ/mol). This is due to an identical electronic configuration at the Mn−O moiety, with the only difference being the spin alignment at the radical on the substrate (antiferromagnetically coupled $\overset{\uparrow\uparrow\uparrow\uparrow}{Mn^{III}}—\overset{\downarrow\bullet}{O}$) to the ferromagnetic state $\overset{\uparrow\uparrow\uparrow\uparrow}{Mn^{III}}—\overset{\uparrow\bullet}{O}$. With regard to the formation of **RC′$_{Fe}$**, a spin crossover from triplet to quintet surface is observed (which is expected to take place at the C−H bond activation transition state) with the formation energy calculated to be exergonic by −11.5 kJ/mol for ^{5}**RC′$_{Fe}$** relative to the preceding reactant complex (^{3}**RC$_{Fe}$**). The quantum theory of atoms in molecules (QTAIM) analysis (Figure S5) reveals that the difference in the formation energy stems from the relatively stronger stabilizing hydrogen/halogen bonding interactions between the substrate and catalyst/HOTf in ^{5}**RC′$_{Fe}$**, with a total hydrogen/halogen bond energy of 209.9 kJ/mol compared to ^{6}**RC′$_{Mn}$**, which exhibits a total hydrogen/halogen bond

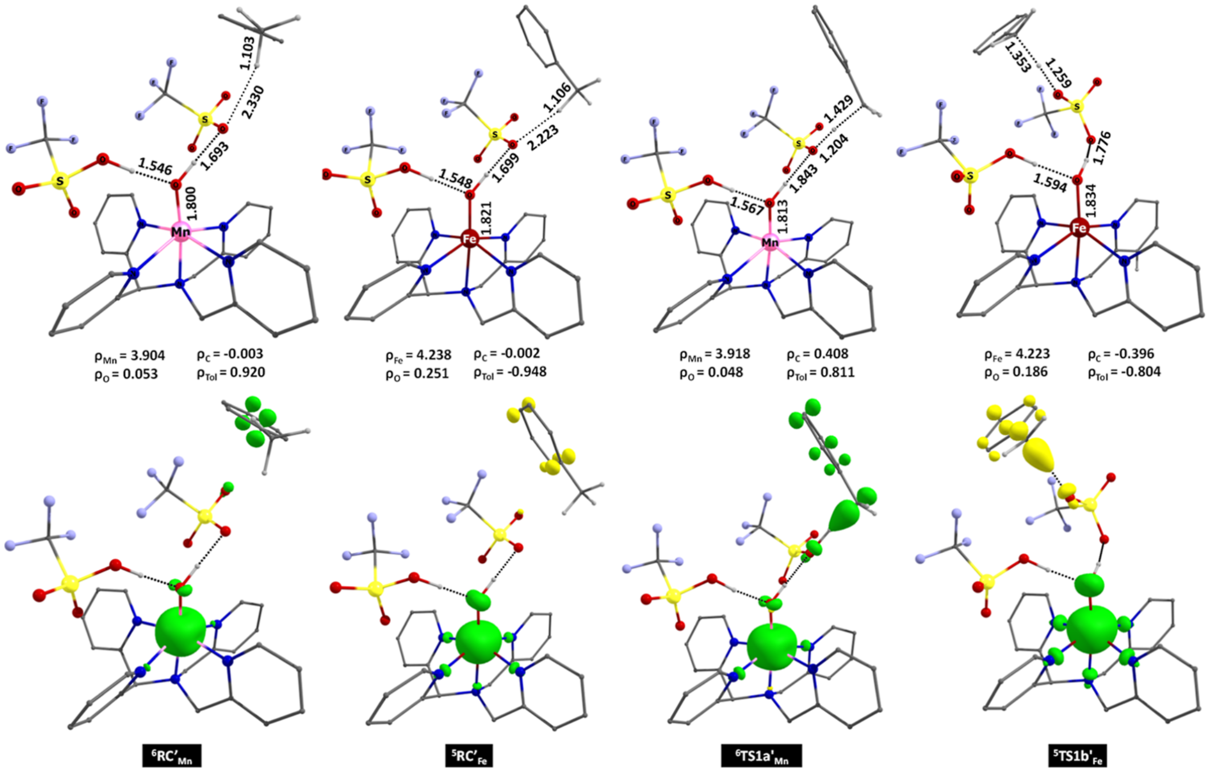

Figure 7. Optimized geometries of ^{6}**RC′**$_{\mathrm{Mn}}$, ^{5}**RC′**$_{\mathrm{Fe}}$, ^{6}**TS1a′**$_{\mathrm{Mn}}$, and ^{5}**TS1b′**$_{\mathrm{Fe}}$ with structural parameters (bond lengths in Å) and their corresponding spin density plots.

energy of 236.7 kJ/mol. Interestingly, analysis of the spin density plots of **RC′**$_{\mathrm{M}}$ (see Figure 7) shows that a one-electron transfer had already occurred from toluene to the metal center in both ^{6}**RC′**$_{\mathrm{Mn}}$ and ^{5}**RC′**$_{\mathrm{Fe}}$ even before the C−H bond of toluene was activated. Around 92.0% of spin-down electrons have been transferred to the Mn center, while 94.8% of the spin-up electrons have been transferred to the Fe center. Upon analyzing the eigenvalue plots of ^{6}**RC′**$_{\mathrm{Mn}}$ and ^{5}**RC′**$_{\mathrm{Fe}}$ (Figure S6), the β-electron is found to be transferred from toluene to d_{xy} orbital of Mn in ^{6}**RC′**$_{\mathrm{Mn}}$ while a spin-up electron is transferred to the $d_{z}{}^{2}$ orbital of the Fe center in ^{5}**RC′**$_{\mathrm{Fe}}$. This choice of ^{6}**RC′**$_{\mathrm{Mn}}$ to abstract a spin-down electron to a nonbonding d_{xy} orbital of Mn rationalizes the experimentally observed outer sphere electron transfer (OSET) mechanism while a spin-up electron transfer from toluene to $d_{z}{}^{2}$ orbital of Fe center via HOTf molecule accounts for the inner sphere electron transfer (ISET) mechanism observed for ^{5}**RC′**$_{\mathrm{Fe}}$.[88]

In the following step, instead of metal−oxo moiety abstracting a hydrogen atom from toluene (as seen in pathways 1 and 2), here the deprotonated triflate anion ($^{-}$OTf) is considered to aid the C−H activation process by abstracting a proton from toluene either through **TS1a′**$_{\mathrm{M}}$ or **TS1b′**$_{\mathrm{M}}$, as depicted in Scheme 2. The transition state **TS1a′**$_{\mathrm{M}}$ describes the abstraction of proton from toluene by one of the sulfonyl oxygen (S = O) atoms of $^{-}$OTf ion while **TS1b′**$_{\mathrm{M}}$ describes the proton transfer from toluene to the deprotonated oxygen atom of $^{-}$OTf ion which is in hydrogen bonding with the metal-hydroxyl moiety. For **1-(HOTf)**$_{2}$, the ^{6}**TS1a′**$_{\mathrm{Mn}}$ surface is the ground state with an estimated barrier height of 40.7 kJ/mol, while ^{4}**E**$_{1}$**-1-TS1a′**$_{\mathrm{Mn}}$ lies close at 42.0 kJ/mol (see Figure 6). This suggests that the proton transfer via ^{4}**E**$_{1}$**-1-TS1a′**$_{\mathrm{Mn}}$ and ^{6}**TS1a′**$_{\mathrm{Mn}}$ requires nearly similar activation free energy. The computed results clearly reveal that the mediation of HOTf (40.7 kJ/mol at ^{6}**TS1a′**$_{\mathrm{Mn}}$) remarkably reduces the barrier by around 20 kJ/mol compared to conventional direct C−H activation (in the absence of HOTf) requiring 66.6 kJ/mol for ^{4}**E**$_{1}$**-1-TS1**$_{\mathrm{Mn}}$. Thus, with a steep barrier in the absence of HOTf, a sluggish reactivity at the experimental conditions is witnessed. It is important to note here that the experimental rate constant (K_{obs}) for HMB bond-dissociation energy (BDE) (339 kJ/mol) possessing slightly lower BDE compared to toluene (BDE ∼ 356 kJ/mol) is 6.7×10^{2} M^{-1} S^{1-} with HOTf and 2.1×10^{-2} M^{-1} S^{1-} in the absence of HOTf, supporting these mechanistic considerations.[89]

While DFT calculations clearly favor the HOTf-mediated C−H bond activation mechanism, indicating lower kinetic barriers, we further extended the study to $\mathrm{Mn^{IV}{=}O}$ by computing the corresponding barrier heights using CASSCF calculations, as described in previous work.[78] These results also support the HOTf-mediated pathway, reinforcing earlier suggestions.[75−77]

For **2-(HOTf)**$_{2}$, the kinetic barrier on the quintet surface (^{5}**TS1b′**$_{\mathrm{Fe}}$) is calculated as the ground state, with an activation free energy of 46.6 kJ/mol. This value is 6.6 kJ/mol lower than the barrier for C−H activation with HOTf as a spectator (53.2 kJ/mol for ^{5}**TS1**$_{\mathrm{Fe}}$) and 28.1 kJ/mol lower than the barrier for direct activation without HOTf (74.7 kJ/mol for ^{5}**TS1**$_{\mathrm{Fe}}$). These results substantiate that the abstraction of a proton from cationic radical toluene by −OTf ion is kinetically more favorable than the direct abstraction of hydrogen atoms by the metal-oxo moiety. The difference in barrier computed with and without HOTf of ∼28 kJ/mol also agrees with the experimental rate reported for the toluene substrate (K_{obs} 1.5×10^{-4} $\mathrm{M}^{-1}\mathrm{S}^{1-}$ without HOTf vs 6.5×10^{-4} M^{-1} S^{1-} with HOTf) where a reasonable enhancement is seen in reactivity in the presence of HOTf.[26] The bond parameters in ^{6}**RC′**$_{\mathrm{Mn}}$ and ^{5}**RC′**$_{\mathrm{Fe}}$ are (Figure 7) found to be similar to the C−H activation transition state computed with HOTf as the spectator (^{6}**TS1**$_{\mathrm{Mn}}$ and

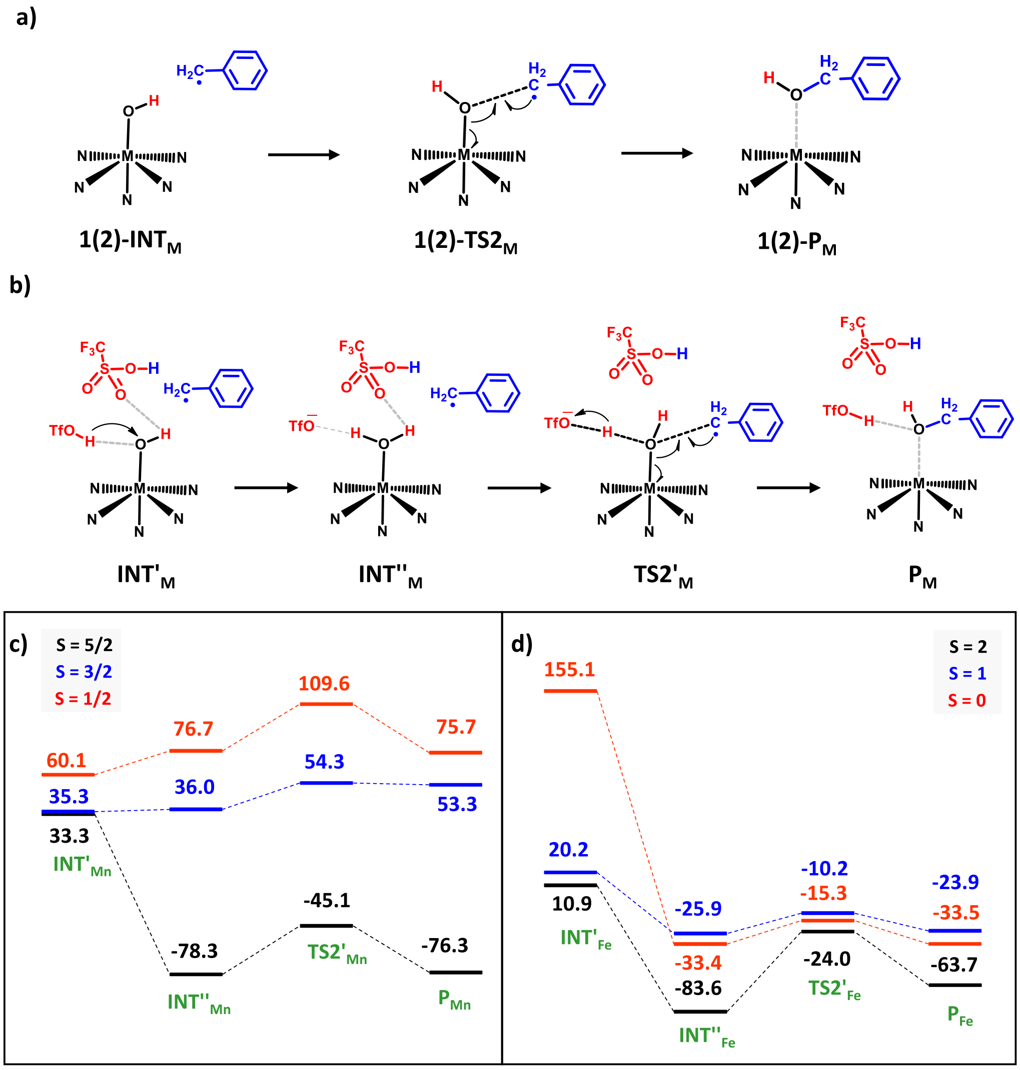

Figure 8. (a) Conventional mechanism of the hydroxyl rebound process, (b) proposed mechanism for HOTf-assisted hydroxyl rebound, and (c) calculated free energy profiles (in kJ/mol) for the HOTf-mediated hydroxyl rebound process catalyzed by **1-(HOTf)$_2$** and (d) by **2-(HOTf)$_2$**.

^{5}**TS1**$_{Fe}$). The metal−oxo bond is found to be elongated to 1.800 and 1.820 Å in ^{6}**RC′**$_{Mn}$ and ^{5}**RC′**$_{Fe}$, respectively. A similar M−O bond length is maintained in the subsequent transition state as well (^{6}**TS1a′**$_{Mn}$ and ^{5}**TS1b′**$_{Fe}$). A relatively shorter hydrogen bonding interaction (in the range of 1.540 Å) is witnessed in the case of nonparticipating HOTf while the hydrogen bonding interaction between the deprotonated $^-$OTf anion and metal−oxo unit was found to be slightly elongated to around 1.700 Å due to its weak hydrogen bonding interaction with toluene alkyl C−H bond. In ^{6}**TS1a′**$_{Mn}$ and ^{5}**TS1b′**$_{Fe}$, the hydrogen bonding between $^-$OTf anion and metal−oxo unit is further weakened to around 1.840 Å as the triflate ion participates in the C−H activation step by abstracting a proton from toluene.

The computed energy profiles depicted in Figure 6 show that the formation of the intermediates ^{6}**INT′**$_{Mn}$ and ^{5}**INT′**$_{Fe}$ is found to be relatively less endothermic compared to the formation energies calculated for their counterparts in pathway 2 where HOTf acts as spectator (51.1 vs 33.3 kJ/mol in ^{2}**INT**$_{Mn}$ and ^{6}**INT′**$_{Mn}$, respectively; 10.9 vs 17.9 kJ/mol in ^{3}**INT**$_{Fe}$ and ^{5}**INT′**$_{Fe}$, respectively). Similar to the trend observed in formation energies of ^{6}**RC′**$_{Mn}$ and ^{4}**RC′**$_{Mn}$, in the intermediate state as well, the quartet and sextet surfaces lie close to each other with energy difference estimated to be less than 2 kJ/mol. This indicates that from the thermodynamic perspective as well, HOTf-mediated C−H activation is relatively favorable compared to the intermediates formed in the absence of HOTf or as HOTf acting only as a spectator. The only exception is the formation of ^{6}**1-INT**$_{Mn}$ (in pathway 1), which is relatively more favorable than the corresponding counterpart formation energies in pathways 2 and 3 (3.9 vs 51.1 vs 33.3 kJ/mol, for pathways 1, 2 and 3, respectively). Thus, the calculated thermodynamic and kinetic energies clearly envisage that C−H activation via the HOTf-mediated pathway is more favorable than the direct C−H activation pathway (in the absence of HOTf) or with HOTf only acting as a spectator (pathway 2).

3.2. Mechanism of the Hydroxyl Rebound Process.

Now we turn to explore the role of BAs in the second step of toluene hydroxylation, i.e., the hydroxyl rebound reaction. Similar to the C−H activation step discussed above; three possible pathways were investigated for this step as well. As sketched in Figure 8a, the conventional hydroxyl rebound mechanism involves a rebound process between the benzyl radical and the metal-hydroxyl moiety through **1(2)-TS2**$_M$, leading to the formation of a hydroxylated product denoted as **1(2)-P**$_M$. In accordance with the reported computational studies and experimental studies, the rebound process is calculated to be a barrierless pathway for both Mn and Fe complexes in the absence of HOTf (see Figure S7).[86] The formation free energies of ^{6}**1-P**$_{Mn}$ and ^{5}**2-P**$_{Fe}$ are calculated to be highly exergonic by −125.5 kJ/mol and −101.2 kJ/mol, respectively. On the other hand, when HOTf molecules are assumed to remain as spectators in the vicinity of the reaction site, as portrayed in Figure S8a, a kinetic barrier of 29.5 and 40.1 kJ/mol is estimated to be required for rebound step to take place at ^{6}**TS2**$_{Mn}$ and ^{5}**TS2**$_{Fe}$, respectively (see Figure S8b). The optimized geometries of the intermediates ^{2}**INT**$_{Mn}$/^{3}**INT**$_{Fe}$ and the transition states (^{6}**TS2**$_{Mn}$ and ^{5}**TS2**$_{Fe}$), along with their spin density plots are deposited in Figure S9. In both the intermediates and the transition states, strong hydrogen bonding interactions (1.570−1.720 Å) between metal−hydroxyl moiety and the HOTf are found, leading to the accumulation of a large negative natural charge on the O atom of the metal−OH unit (−0.902/−0.966 in ^{2}**INT**$_{Mn}$/^{6}**TS2**$_{Mn}$ and −0.966/-1.021 in ^{3}**INT**$_{Fe}$/^{5}**TS2**$_{Fe}$). The anchoring of the metal−hydroxyl moiety within the strong hydrogen bonding network of HOTf molecules, along with the enhanced anionic character of the corresponding O atom, renders the hydroxyl group more favorable for the abstraction of a proton from one of the HOTf molecules rather than for a rebound reaction with the benzyl radical substrate. This could be reckoned as the possible origin for the estimated kinetic barrier for the hydroxyl rebound step in the presence of HOTf molecules, while their absence facilitates a barrier-less rebound process. This led us to evaluate the possibility of protonation of the metal−hydroxyl group by one of the hydrogen-bonded HOTf molecules to form a metal−OH_2 species (denoted as **INT″**$_{M}$), as depicted in Figure 8b). Interestingly, the calculated formation free energy is found to be highly exergonic by −78.3 kJ/mol for ^{6}**INT″**$_{Mn}$ and −83.6 kJ/mol for ^{5}**INT″**$_{Fe}$ (see Figure 8c). In the ensuing step, the transfer of proton back to the deprotonated triflate ion takes place simultaneously coupled with the rebound of the hydroxyl moiety, as described by **TS2′**$_{M}$ in Figure 8b. The activation free energy barrier for this process is calculated to lie at −45.1 and −24.0 kJ/mol for ^{6}**TS2**$_{Mn}$ and ^{5}**TS2**$_{Fe}$, respectively. The highly exergonic nature of **INT″**$_{M}$ and the relatively low free energy barrier required for **TS2′**$_{M}$ indicate that the HOTf-mediation is essential for the rebound process to take place while HOTf acting only as a spectator would encumber the rebound process as discussed above. The optimized geometries of ^{6}**INT″**$_{Mn}$/^{5}**INT″**$_{Fe}$ and ^{6}**TS2′**$_{Mn}$/^{5}**TS2′**$_{Fe}$ are displayed in Figure S10. Both in the intermediates and in the transition states, significant elongation in the metal−oxygen bond distances is witnessed due to the formation of M−OH_2 species [2.213(2.110) Å/2.303(2.141) vs 1.852(1.879) Å/2.253(2.069) in ^{6}**INT″**$_{Mn}$(^{5}**INT″**$_{Fe}$)/^{6}**TS2′**$_{Mn}$(^{5}**TS2′**$_{Fe}$) and ^{2}**INT**$_{Mn}$(^{3}**INT**$_{Fe}$)/^{6}**TS2**$_{Mn}$(^{5}**TS2**$_{Fe}$), respectively] while the hydrogen bonding interactions are found to be weakened in **INT″**$_{M}$/**TS2′**$_{M}$ (1.670 Å to 1.850 Å) than those in **INT**$_{M}$/**TS2**$_{M}$ (1.570 Å to 1.720 Å). This is also reflected in the relatively shorter bond distance between the substrate carbon radical and the O atom of M−OH_2 unit in ^{6}**TS2′**$_{Mn}$ and ^{5}**TS2′**$_{Fe}$ (1.967 and 2.116 Å) compared to the same in ^{6}**TS2**$_{Mn}$ and ^{5}**TS2**$_{Fe}$ (2.061 and 2.212 Å). These structural and electronic changes facilitate the easy rebound process and provide a rationale for the decreased kinetic energy expense for the HOTf-mediated rebound process.

4. DISCUSSION

4.1. Mechanistic Considerations and Correlation to Experiments. The overall free energy profile comparing the ground state energies of all putative intermediates and transition states involved in all three pathways for both C−H activation and hydroxyl rebound steps is presented in Figure 9. In all pathways, the C−H activation step is the rds in accordance with the experimental reports.[88] From the energy profile, it is clear that pathway 3 is the minimum energy route throughout the mechanism except for the formation of ^{6}**1-INT**$_{Mn}$ in Figure 9a and the products. This demonstrates that the addition of HOTf to the reaction mixture drastically decreases the activation barrier for C−H activation by actively participating as a shuttle between the substrate and the catalyst. The important mechanistic changes brought about by HOTf in the C−H activation step are enlisted below in comparison with the conventional C−H activation mechanism in Table 1. The HOTf-mediated C−H activation occurs in two stages. Initially, it protonates the metal−oxo moiety, leading to the formation of M−OH species and triflate anion; this favors the formation of ion-pair with toluene by one-electron reduction leading to

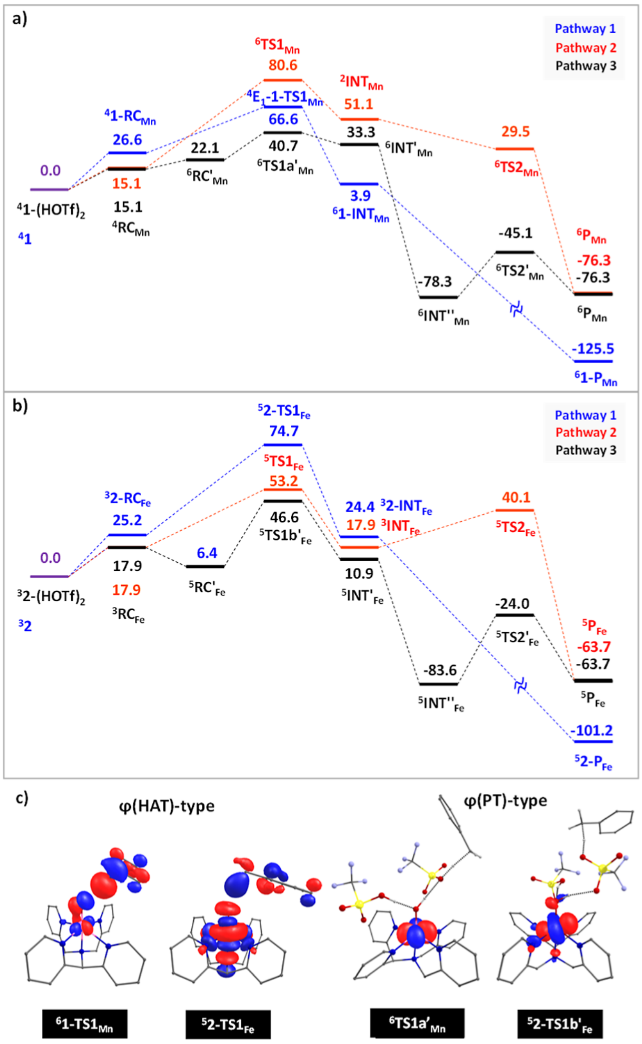

Figure 9. Comparative free energy profiles (in kJ/mol) for toluene hydroxylation via pathways 1, 2, and 3 catalyzed by (a) ^{4}**1**/^{4}**1-(HOTf)**$_{2}$ and (b) ^{3}**2**/^{3}**2-(HOTf)**$_{2}$. (c) Pertinent spin natural orbitals (SNOs).

Table 1. Key Mechanistic Changes between Conventional and HOTf-Mediated C−H Activation

conventional C−H activation (without HOTf)	HOTf-mediated C−H activation
a. M−O bond has a significant radical character, suggesting a favorable HAT mechanism	a. M−O bond radical character diminishes, and the negative charge on O increases by ∼0.2e unit, tilting the reaction toward the PCET process
b. Both proton and electron transfer occur from the substrate to the M−oxo species	b. Proton transfer occurs from HOTf to M−oxo while electron transfer (long-range) occurs from the substrate to the M−oxo moiety simultaneously
c. C−H bond of toluene is activated at its neutral state	c. C−H bond of toluene is activated at its radical cation state
d. The hydrogen atom of the C−H bond is abstracted by the M−oxo moiety	d. Proton from the C−H bond is abstracted by triflate anion and not by metal−oxo species
e. The estimated C−H bond activation barrier lies in the range of 66−90 kJ/mol for **1** and **2**	e. The estimated C−H bond activation barrier drops to around 40 kJ/mol for **1** and **2**
f. −OH rebound is barrier-less for both **1** and **2**	f. −OH rebound has a finite barrier but is eased by the stability of the precedent intermediate

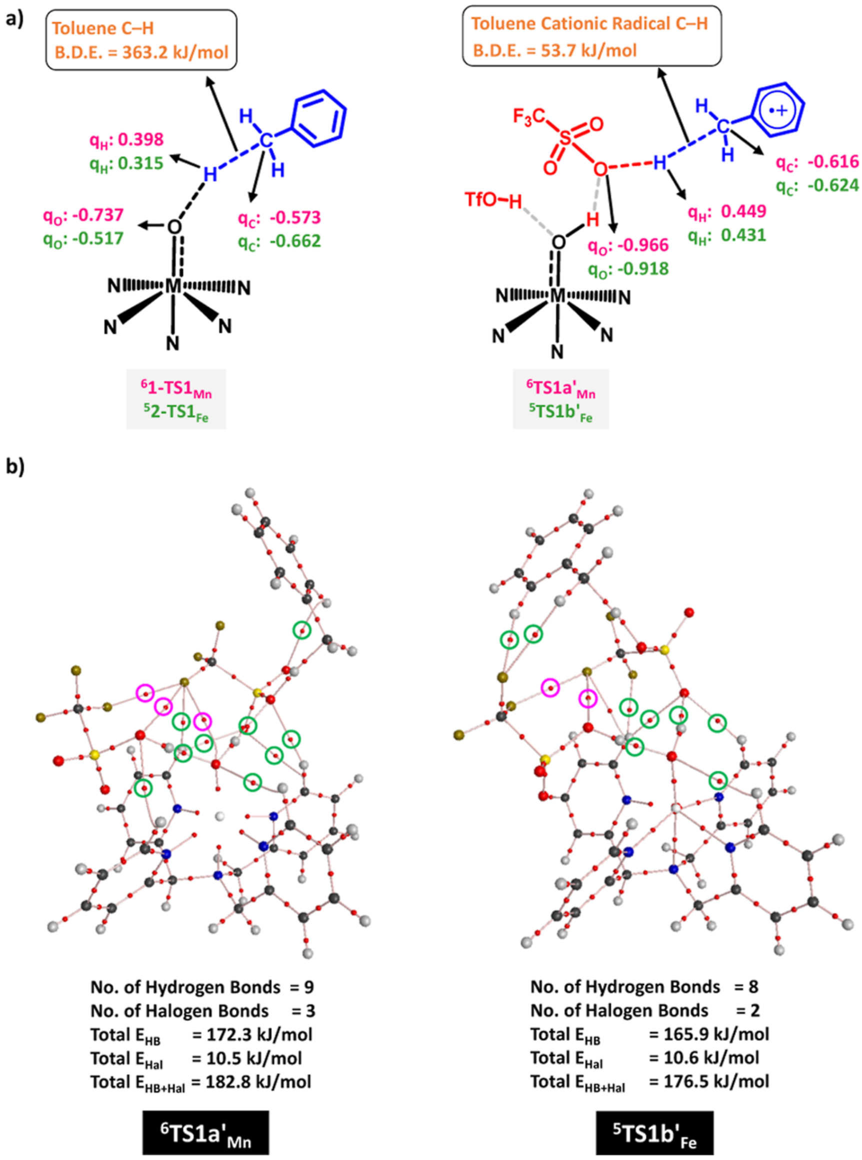

Figure 10. (a) Schematic representation of C−H activation transition states involved in pathways 1 and 3 with relevant natural charges (q) and computed BDE. (b) Molecular graphs of ^{6}**TS1a′**$_{\mathrm{Mn}}$ and ^{5}**TS1b′**$_{\mathrm{Fe}}$ generated from QTAIM analysis. The BCPs circled in green represent hydrogen bonding interactions, while pink circles represent BCPs of halogen bonding interactions.

triflate-anion-toluene-radical-cation formation and concurrent ET to the metal-oxo moiety. Thus, the O−H bond is clearly involved in the rds step, and this is correlated to the inverse KIE observed in the experiments with DOTf acid.[26] The triflate anion in the transition state abstracts the proton from the C−H bond of the substrate to compensate for the initial loss. At this juncture, the substrate carbon (−CH_2) is ∼5.0−7.3 Å (∼2.61−4.27 Å in the absence of HOTf), suggesting a long-range PCET mechanism that exerts little strain both on the substrate and the catalyst. The computed spin natural orbitals (SNOs) provide strong evidence for the HAT versus PCET mechanisms. In the absence of HOTf, σ-type orbital lobes are present on both the

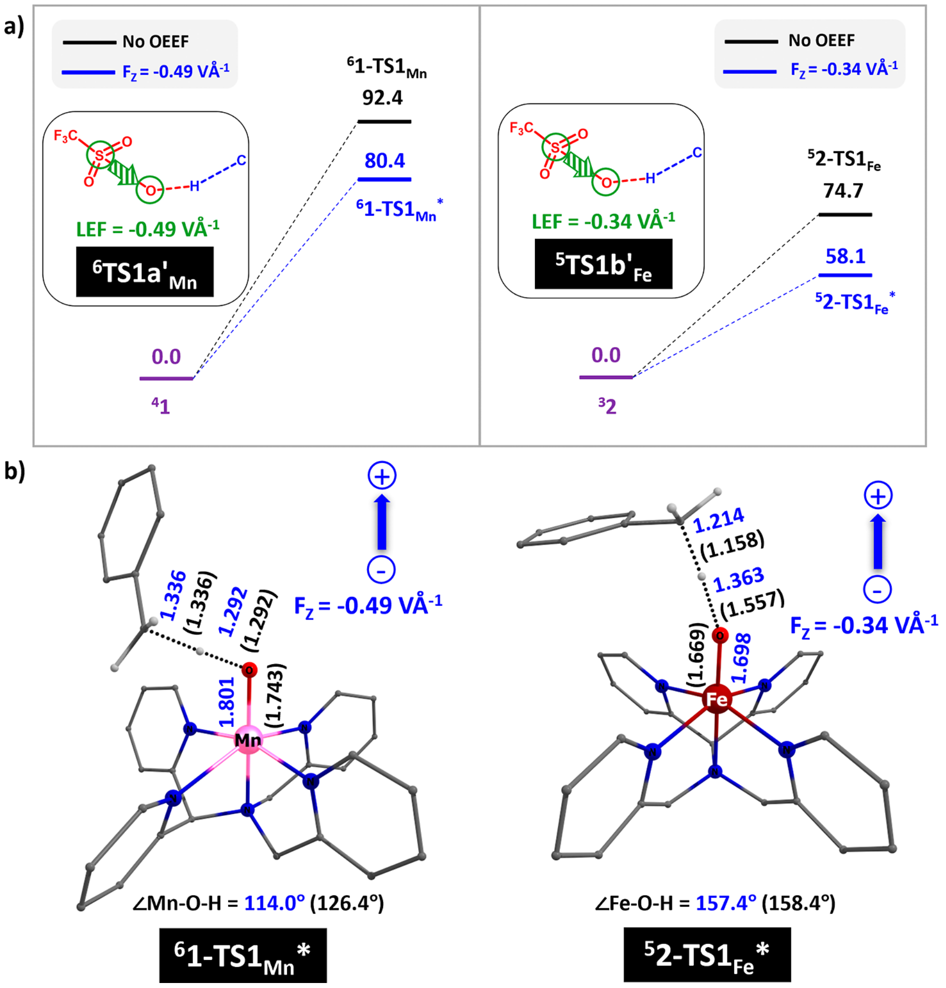

Figure 11. (a) Calculated activation free energies (in kJ/mol) for C−H activation in the presence and absence of OEEF along with the (b) optimized transition-state geometries computed in the presence of OEEF.

oxo group and the methyl radical carbon atom of toluene, with the hydrogen atom located at the nodal point, supporting the HAT mechanism. In contrast, when HOTf is present, no lobes are observed on the substrate, indicating that the contributions arise solely from the metal $d_{xy}/d_{x^2-y^2}$ orbitals (see Figure 9c), thereby confirming the PCET mechanism.

While our mechanism explains the higher reactivity for Brønsted acids (BA), the situation for LA is less clear and cannot be directly extended. Many metal-oxo species, including the ones studied here, show enhanced reactivity for both BA and LA. In this context, it is noteworthy that Browne and co-workers[90] have shown that LA like Sc(OTf)$_3$ can generate BAs (HOTf) in acetonitrile, even in its dry form, with HOTf formation detected. Comparing the reactivity of HMB with Fe(IV)=O species in the presence of Sc(OTf)$_3$ and HOTf reveals a dramatic increase in rate constants (420 times higher with HOTf). These findings suggest that Sc(OTf)$_3$ likely plays an indirect role, facilitating the generation of HOTf, which then acts as an active catalytic species. Thus, the mechanistic findings have larger implications.

4.2. Driving Force Behind Drastic Enhancement of Rate in the Presence of HOTf. Our investigation into the cause of the lower barrier in the presence of HOTf indicates a variation in the BDE of toluene. As sextet state is the ground state for the HOTf-assisted transition state (^{6}**TS1a′**$_{\mathbf{Mn}}$), we have here compared the corresponding ^{6}**1-TS1**$_{\mathbf{Mn}}$ transition state for further discussions.

For the neutral toluene molecule, the BDE of the methyl C−H bond is estimated to be 363.2 kJ/mol. However, in its cation radical state, as observed in the presence of HOTf, this value drops significantly to 53.7 kJ/mol (Figure 10a). Furthermore, NBO analysis reveals that the methyl C−H bond is highly polarized in toluene cationic radical with a large positive charge on the H atom (0.449/0.431) compared to the same in its neutral analogue (0.398/0.315). In addition, the O atom of the triflate anion was found to have a large negative charge (−0.966/−0.918) compared to the oxyl oxygen (−0.737/−0.517 for 1/2) at **1(2)-TS1**$_{\mathbf{M}}$. This enhanced nucleophilicity of the triflate anionic oxygen triggers facile proton abstraction from the substrate, reducing the barrier effectively.

4.2.1. Role of Noncovalent Interactions. Topological analysis of the ^{6}**TS1a′**$_{\mathbf{Mn}}$ and ^{5}**TS1b′**$_{\mathbf{Fe}}$ was carried out using QTAIM formalism, and the corresponding molecular graphs are shown in Figure 10b. Two types of noncovalent interactions were noted between the substrate and HOTf: (i) (substrate)C−H···F(triflic acid) and (ii) (substrate)C−H···O(triflic acid). Furthermore, several hydrogen bonding interactions between the HOTf and the catalyst with a total interaction energy (E_{HB}) of 172.3 and 165.9 kJ/mol were found in ^{6}**TS1a′**$_{\mathbf{Mn}}$ and ^{5}**TS1b′**$_{\mathbf{Fe}}$, respectively. Interestingly, a few halogen bonding interactions are also observed between the two triflic acids in both transition states with a total interaction energy (E_{Hal}) of ∼10 kJ/mol. The overall interaction energy ($E_{\mathrm{HB+Hal}}$) of all the

https://doi.org/10.1021/acs.inorgchem.4c04948
Inorg. Chem. 2025, 64, 5944−5959

noncovalent interactions sums up to 182.8 kJ/mol in ^{6}**TS1a′**$_{\mathbf{Mn}}$ and 176.5 kJ/mol in ^{5}**TS1b′**$_{\mathbf{Fe}}$. This provides a qualitative picture of the overall stabilization rendered by these noncovalent interactions in the HOTf-mediated C−H activation transition state. The absence of HOTf in direct C−H activation transition states lacks such stabilizing interactions leading to larger barriers.

4.2.2. Energy Decomposition Analysis. To further understand the additional factors that influence the activation barrier, EDA was carried out on ^{6}**1-TS1**$_{\mathbf{Mn}}$, ^{5}**2-TS1**$_{\mathbf{Fe}}$, ^{6}**TS1a′**$_{\mathbf{Mn}}$, and ^{5}**TS1b′**$_{\mathbf{Fe}}$ by considering the complex, substrate, and each of the two HOTf molecules as separate fragments, as depicted in Table S1. The steric energy (ΔE_{Steric}) is estimated to be 1.42 and 2.10 times larger in ^{6}**TS1a′**$_{\mathbf{Mn}}$ and ^{5}**TS1b′**$_{\mathbf{Fe}}$, respectively, compared to the corresponding transition state without HOTf molecules (in pathway 1). On the other hand, the orbital interaction energy (ΔE_{orb}) is computed to be equally large as well in the HOTf-mediated transition state than their analogues in pathway 1 (1.43 times more in ^{6}**TS1a′**$_{\mathbf{Mn}}$ than ^{6}**1-TS1**$_{\mathbf{Mn}}$ and 2.17 times more in ^{5}**TS1b′**$_{\mathbf{Fe}}$ than that in ^{5}**2-TS1**$_{\mathbf{Fe}}$). The resultant net stabilizing interaction energy (ΔE_{Int}) is calculated to be larger in ^{6}**TS1a′**$_{\mathbf{Mn}}$, and ^{5}**TS1b′**$_{\mathbf{Fe}}$ (around −280 kJ/mol) compared to ^{6}**1-TS1**$_{\mathbf{Mn}}$ and ^{5}**1-TS1**$_{\mathbf{Fe}}$ (−185.6 kJ/mol and −14.6 kJ/mol). This signifies that the HOTf interaction in the C−H activation process is found to add significant stabilization to the transition state, leading to a lower activation barrier than that in the absence of HOTf molecules.

4.2.3. Effect of Local Electric Fields. Recently, Styver and Shaik co-workers have demonstrated that the LEF generated in charged complexes plays a decisive role in enhancing the reaction rates for the hydrogen abstraction reaction compared to their neutral analogues relevant to the action of metalloenzymes like Compound I (Cpd I) and synthetic hydroxo ferric species.[91] In this study, since charged species such as triflate anion and toluene cation radical are involved in the HOTf-mediated C−H activation process, we assess the impact of the LEF to understand its role in shaping the activation barrier. In this regard, the LEF oriented along the S−O bond participating in the C−H activation process was estimated in ^{6}**TS1a′**$_{\mathbf{Mn}}$/^{5}**TS1b′**$_{\mathbf{Fe}}$ and compared with the LEF along the M−O bond in a direct C−H activation transition state. The net LEF along the S−O bond was computed to be −0.49 V Å^{-1} and −0.34 V Å^{-1} for ^{6}**TS1a′**$_{\mathbf{Mn}}$ and ^{5}**TS1b′**$_{\mathbf{Fe}}$, respectively. However, the LEF along M−O bond in direct C−H activation transition state is found to be remarkably lower (0.54 V Å^{-1} and −0.05 V Å^{-1} for ^{6}**1-TS1**$_{\mathbf{Mn}}$ and ^{5}**2-TS1**$_{\mathbf{Fe}}$, respectively). To substantiate that the charge group around the catalysis offer LEF and lowers the barrier, the computed LEF of the S−O bond is physically applied along the z-axis of ^{6}**1-TS1**$_{\mathbf{Mn}}$ and ^{5}**2-TS1**$_{\mathbf{Fe}}$ (aligned with M−O bond) and the transition state in the presence of this oriented external electric field (OEEF) is computed. The free energy barrier computed with OEEF is found to be 80.4 and 58.1 kJ/mol for ^{6}**1-TS1**$_{\mathbf{Mn}}$* and ^{5}**2-TS1**$_{\mathbf{Fe}}$*, respectively (Figure 11a), which is 12.0 and 16.6 kJ/mol lower than their corresponding analogues with no OEEF (^{6}**1-TS1**$_{\mathbf{Mn}}$ and ^{5}**2-TS1**$_{\mathbf{Fe}}$). From Figure 11b, it can be seen that the metal−oxo bonds are elongated along the Z-axis due to the applied OEEF from 1.743 Å in ^{6}**1-TS1**$_{\mathbf{Mn}}$ to 1.801 Å in ^{6}**1-TS1**$_{\mathbf{Mn}}$* and from 1.669 Å in ^{5}**2-TS1**$_{\mathbf{Fe}}$ to 1.698 Å in ^{5}**2-TS1**$_{\mathbf{Fe}}$*. This enables efficient hydrogen atom abstraction from toluene by the metal-oxo moiety and may also contribute to decreasing the steric interactions between the substrate and the catalyst. Earlier reactivity studies on Fe$^{\text{IV}}$═O and Fe$^{\text{IV}}$═NTs species indicate that steric interactions with the pyridinic hydrogen atoms are crucial for reactivity.[43] In our case, although the hydrogen atoms in both catalysts are aligned in the same direction, the metal-oxo bond lengths differ, suggesting that catalyst **2** experiences stronger steric interactions compared to catalyst **1**. Thus, replicating the LEF found along the S−O bond in the triflate anion and applying it to the M−O bond result in a considerable reduction in the activation energy. This suggests that the LEF generated due to the charged triflate anion and cationic radical toluene is also one of the driving forces for the faster reaction in the presence of HOTf.

4.2.4. Approach to De Novo Catalyst Design. Based on the aforementioned mechanistic insights, the following approach can be adapted to enhance the catalytic efficiency: (i) a larger charge on the BA is expected to produce larger LEF and also will have a greater ability to perform PCET; (ii) choice of the substrate where the produced cationic charge is localized rather than strongly delocalized as seen in toluene is expected to generate larger dipole and hence greater LEF; (iii) stronger polar protic solvents likely to enhance the dipole and generate larger LEF and reduce the barrier height; and (iv) enhancing the number of noncovalent interactions between BA and the substrate via appropriate donor−acceptor design.

5. CONCLUSIONS

A detailed computational investigation has been carried out to understand the mechanistic aspects of BA-promoted C−H activation by using [(N4Py)Mn$^{\text{IV}}$(O)]$^{2+}$ (**1**) and [(N4Py)-Fe$^{\text{IV}}$(O)]$^{2+}$ (**2**) and their corresponding BA-bound analogues (**1**-**(HOTf)**$_2$ and **2**-**(HOTf)**$_2$) as representative nonheme metal−oxo models with toluene as the substrate and triflic acid as the BA. Below is a summary of key conclusions from this study:

(i) Our calculations show that in the absence of HOTf, the rate-determining C−H activation step for both **1** and **2** requires high activation energies of 66.6 and 74.7 kJ/mol, respectively. When HOTf molecules act as spectators near the reaction site, the energy barrier increases by ∼15 kJ/mol for **1** and decreases by 20 kJ/mol for **2**. However, when HOTf actively participates in promoting the PCET reaction, the computed barriers drop significantly to 40.7 kJ/mol for **1**-**(HOTf)**$_2$ and 46.6 kJ/mol for **2**-**(HOTf)**$_2$, accounting for the experimentally observed BA-enhanced reaction rates.

(ii) The mechanistic origin for the decreased activation barrier due to HOTf-mediation is found to occur in two stages: first, HOTf triggers the electron transfer from toluene by protonating the metal−oxo moiety, resulting in the formation of the toluene cationic radical and triflate anion. In the second stage, the anionic triflate ion performs the C−H bond activation and not the metal-oxo moiety as the conventional mechanism demands, triggering a PCET mechanism as opposed to the conventional HAT mechanism.

(iii) Various factors contribute to the rate enhancement in the presence of BA: (a) lower BDE of the methyl C−H bond of the toluene cation radical generated by the HOTf, (b) high nucleophilicity of the oxygen atom of the triflate anion and its greater tendency to abstract a proton from the substrate, (c) the LEF generated by the HOTf molecule (10−20 kJ/mol reduction), and (d) presence of large number of noncovalent interactions between the

HOTf and the catalyst and also between the HOTf and substrate (they ease, the energy penalty).

(iv) In the hydroxyl rebound step, the absence of HOTf allows for a barrier-less rebound process. However, when HOTf acts as a spectator, it mildly obstructs the rebound by forming strong hydrogen bonds with the M−OH moiety, raising the activation energy by ∼30−40 kJ/mol. In contrast, when HOTf participates by protonating M−OH to form M−OH_2, it facilitates the rebound process, making it highly exergonic at the rebound transition state.

In summary, our computational study reveals the unexpected and pivotal role of BA, specifically triflic acid, in directly seizing the C−H bonds of the activated substrate, working in tandem with the catalyst. This unusual mechanism offers new insights into catalytic design and reactivity and sets the stage for future breakthroughs in enzyme and synthetic catalyst design.

■ ASSOCIATED CONTENT

Supporting Information

The Supporting Information is available free of charge at https://pubs.acs.org/doi/10.1021/acs.inorgchem.4c04948.

FMOs responsible for the origin of the computed absorption band at 562 nm for **1-(HOTf)$_2$**; optimized geometries with structural parameters (bond lengths in Å and bond angles in °) and their corresponding spin density plots of relevant species; scan plots for proton transfer from **RC$_M$** to **RC′$_M$** formation; molecular graphs of **^{6}RC′$_{Mn}$** and **^{5}RC′$_{Fe}$** calculated from QTAIM analysis; UB3LYP-D3 computed FMO diagram of **^{6}RC′$_{Mn}$** and **^{5}RC′$_{Fe}$**; conventional mechanism of hydroxyl rebound process and their corresponding calculated free energy profiles (in kJ/mol) for the same catalyzed by **1**, **2**, **1-(HOTf)$_2$** and **2-(HOTf)$_2$**; and EDA data (PDF)

■ AUTHOR INFORMATION

Corresponding Authors

Gopalan Rajaraman − *Department of Chemistry, Indian Institute of Technology Bombay, Mumbai 400 076, India;* orcid.org/0000-0001-6133-3026; Email: rajaraman@chem.iitb.ac.in

Neethinathan Johnee Britto − *Department of Chemistry, Indian Institute of Technology Bombay, Mumbai 400 076, India;* orcid.org/0000-0001-9447-022X; Email: johneebritto@gmail.com

Author

Asmita Sen − *Department of Chemistry, Indian Institute of Technology Bombay, Mumbai 400 076, India*

Complete contact information is available at: https://pubs.acs.org/10.1021/acs.inorgchem.4c04948

Author Contributions

All authors have given approval to the final version of the manuscript.

Funding

DST and SERB (SB/SJF/2019-20/12; CRG/2022/001697).

Notes

The authors declare no competing financial interest.

■ ACKNOWLEDGMENTS

N.J.B. and A.S. thank IITB for the postdoctoral fellowship.

■ REFERENCES

(1) Hong, S.; Lee, Y.-M.; Cho, K.-B.; Sundaravel, K.; Cho, J.; Kim, M. J.; Shin, W.; Nam, W. Ligand Topology Effect on the Reactivity of a Mononuclear Nonheme Iron(IV)-Oxo Complex in Oxygenation Reactions. *J. Am. Chem. Soc.* **2011**, *133* (31), 11876−11879.

(2) Tang, H.; Guan, J.; Zhang, L.; Liu, H.; Huang, X. The Effect of the Axial Ligand on Distinct Reaction Tunneling for Methane Hydroxylation by Nonheme Iron(Iv)−Oxo Complexes. *Phys. Chem. Chem. Phys.* **2012**, *14* (37), 12863−12874.

(3) Kumar, D.; Sastry, G. N.; de Visser, S. P. Axial Ligand Effect On The Rate Constant of Aromatic Hydroxylation By Iron(IV)−Oxo Complexes Mimicking Cytochrome P450 Enzymes. *J. Phys. Chem. B* **2012**, *116* (1), 718−730.

(4) Chiavarino, B.; Cipollini, R.; Crestoni, M. E.; Fornarini, S.; Lanucara, F.; Lapi, A. Probing the Compound I-like Reactivity of a Bare High-Valent Oxo Iron Porphyrin Complex: The Oxidation of Tertiary Amines. *J. Am. Chem. Soc.* **2008**, *130* (10), 3208−3217.

(5) Kaizer, J.; Klinker, E. J.; Oh, N. Y.; Rohde, J.-U.; Song, W. J.; Stubna, A.; Kim, J.; Münck, E.; Nam, W.; Que, L. Nonheme FeIVO Complexes That Can Oxidize the C−H Bonds of Cyclohexane at Room Temperature. *J. Am. Chem. Soc.* **2004**, *126* (2), 472−473.

(6) Sacramento, J. J. D.; Goldberg, D. P. Factors Affecting Hydrogen Atom Transfer Reactivity of Metal−Oxo Porphyrinoid Complexes. *Acc. Chem. Res.* **2018**, *51* (11), 2641−2652.

(7) Mandal, D.; Mallick, D.; Shaik, S. Kinetic Isotope Effect Determination Probes the Spin of the Transition State, Its Stereochemistry, and Its Ligand Sphere in Hydrogen Abstraction Reactions of Oxoiron(IV) Complexes. *Acc. Chem. Res.* **2018**, *51* (1), 107−117.

(8) Cook, S. A.; Borovik, A. S. Molecular Designs for Controlling the Local Environments around Metal Ions. *Acc. Chem. Res.* **2015**, *48* (8), 2407−2414.

(9) Loll, B.; Kern, J.; Saenger, W.; Zouni, A.; Biesiadka, J. Towards Complete Cofactor Arrangement in the 3.0 Å Resolution Structure of Photosystem II. *Nature* **2005**, *438* (7070), 1040−1044.

(10) Umena, Y.; Kawakami, K.; Shen, J.-R.; Kamiya, N. Crystal Structure of Oxygen-Evolving Photosystem II at a Resolution of 1.9 Å. *Nature* **2011**, *473* (7345), 55−60.

(11) Liu, Y.; Lau, T.-C. Activation of Metal Oxo and Nitrido Complexes by Lewis Acids. *J. Am. Chem. Soc.* **2019**, *141* (9), 3755−3766.

(12) Tsui, E. Y.; Tran, R.; Yano, J.; Agapie, T. Redox-Inactive Metals Modulate the Reduction Potential in Heterometallic Manganese−Oxido Clusters. *Nat. Chem.* **2013**, *5* (4), 293−299.

(13) Sankaralingam, M.; Lee, Y.-M.; Pineda-Galvan, Y.; Karmalkar, D. G.; Seo, M. S.; Jeon, S. H.; Pushkar, Y.; Fukuzumi, S.; Nam, W. Redox Reactivity of a Mononuclear Manganese-Oxo Complex Binding Calcium Ion and Other Redox-Inactive Metal Ions. *J. Am. Chem. Soc.* **2019**, *141* (3), 1324−1336.

(14) Bae, S. H.; Lee, Y.-M.; Fukuzumi, S.; Nam, W. Fine Control of the Redox Reactivity of a Nonheme Iron(III)−Peroxo Complex by Binding Redox-Inactive Metal Ions. *Angew. Chem., Int. Ed.* **2017**, *56* (3), 801−805.

(15) Zhang, Z.; Coats, K. L.; Chen, Z.; Hubin, T. J.; Yin, G. Influence of Calcium(II) and Chloride on the Oxidative Reactivity of a Manganese(II) Complex of a Cross-Bridged Cyclen Ligand. *Inorg. Chem.* **2014**, *53* (22), 11937−11947.

(16) Hong, S.; Lee, Y.-M.; Sankaralingam, M.; Vardhaman, A. K.; Park, Y. J.; Cho, K.-B.; Ogura, T.; Sarangi, R.; Fukuzumi, S.; Nam, W. A Manganese(V)−Oxo Complex: Synthesis by Dioxygen Activation and Enhancement of Its Oxidizing Power by Binding Scandium Ion. *J. Am. Chem. Soc.* **2016**, *138* (27), 8523−8532.

(17) Morimoto, Y.; Park, J.; Suenobu, T.; Lee, Y.-M.; Nam, W.; Fukuzumi, S. Mechanistic Borderline of One-Step Hydrogen Atom Transfer versus Stepwise Sc3+-Coupled Electron Transfer from Benzyl Alcohol Derivatives to a Non-Heme Iron(IV)-Oxo Complex. *Inorg. Chem.* **2012**, *51* (18), 10025−10036.

(18) Park, J.; Morimoto, Y.; Lee, Y.-M.; You, Y.; Nam, W.; Fukuzumi, S. Scandium Ion-Enhanced Oxidative Dimerization and N-Demethy-

lation of N,N-Dimethylanilines by a Non-Heme Iron(IV)-Oxo Complex. *Inorg. Chem.* **2011**, *50* (22), 11612−11622.

(19) Park, J.; Morimoto, Y.; Lee, Y.-M.; Nam, W.; Fukuzumi, S. Metal Ion Effect on the Switch of Mechanism from Direct Oxygen Transfer to Metal Ion-Coupled Electron Transfer in the Sulfoxidation of Thioanisoles by a Non-Heme Iron(IV)−Oxo Complex. *J. Am. Chem. Soc.* **2011**, *133* (14), 5236−5239.

(20) Morimoto, Y.; Kotani, H.; Park, J.; Lee, Y.-M.; Nam, W.; Fukuzumi, S. Metal Ion-Coupled Electron Transfer of a Nonheme Oxoiron(IV) Complex: Remarkable Enhancement of Electron-Transfer Rates by Sc3+. *J. Am. Chem. Soc.* **2011**, *133* (3), 403−405.

(21) Chen, Z.; Yang, L.; Choe, C.; Lv, Z.; Yin, G. Non-Redox Metal Ion Promoted Oxygen Transfer by a Non-Heme Manganese Catalyst. *Chem. Commun.* **2015**, *51* (10), 1874−1877.

(22) Park, Y. J.; Ziller, J. W.; Borovik, A. S. The Effects of Redox-Inactive Metal Ions on the Activation of Dioxygen: Isolation and Characterization of a Heterobimetallic Complex Containing a MnIII−(μ-OH)−CaII Core. *J. Am. Chem. Soc.* **2011**, *133* (24), 9258−9261.

(23) Kanady, J. S.; Tsui, E. Y.; Day, M. W.; Agapie, T. A Synthetic Model of the Mn3Ca Subsite of the Oxygen-Evolving Complex in Photosystem II. *Science (80-.)* **2011**, *333* (6043), 733−736.

(24) Fukuzumi, S. Electron Transfer and Catalysis with High-Valent Metal-Oxo Complexes. *Dalton Trans.* **2015**, *44* (15), 6696−6705.

(25) Chen, J.; Lee, Y.-M.; Davis, K. M.; Wu, X.; Seo, M. S.; Cho, K.-B.; Yoon, H.; Park, Y. J.; Fukuzumi, S.; Pushkar, Y. N.; et al. A Mononuclear Non-Heme Manganese(IV)−Oxo Complex Binding Redox-Inactive Metal Ions. *J. Am. Chem. Soc.* **2013**, *135* (17), 6388−6391.

(26) Park, J.; Morimoto, Y.; Lee, Y.-M.; Nam, W.; Fukuzumi, S. Unified View of Oxidative C−H Bond Cleavage and Sulfoxidation by a Nonheme Iron(IV)−Oxo Complex via Lewis Acid-Promoted Electron Transfer. *Inorg. Chem.* **2014**, *53* (7), 3618−3628.

(27) Yoon, H.; Lee, Y.-M.; Wu, X.; Cho, K.-B.; Sarangi, R.; Nam, W.; Fukuzumi, S. Enhanced Electron-Transfer Reactivity of Nonheme Manganese(IV)−Oxo Complexes by Binding Scandium Ions. *J. Am. Chem. Soc.* **2013**, *135* (24), 9186−9194.

(28) Kal, S.; Que, Jr. L. Activation of a Non-Heme FeIII-OOH by a Second FeIII to Hydroxylate Strong C−H Bonds: Possible Implications for Soluble Methane Monooxygenase. *Angew. Chem., Int. Ed.* **2019**, *58* (25), 8484−8488.

(29) Leeladee, P.; Baglia, R. A.; Prokop, K. A.; Latifi, R.; de Visser, S. P.; Goldberg, D. P. Valence Tautomerism in a High-Valent Manganese−Oxo Porphyrinoid Complex Induced by a Lewis Acid. *J. Am. Chem. Soc.* **2012**, *134* (25), 10397−10400.

(30) Karmalkar, D. G.; Sankaralingam, M.; Seo, M. S.; Ezhov, R.; Lee, Y.-M.; Pushkar, Y. N.; Kim, W.-S.; Fukuzumi, S.; Nam, W. A High-Valent Manganese(IV)−Oxo−Cerium(IV) Complex and Its Enhanced Oxidizing Reactivity. *Angew. Chem., Int. Ed.* **2019**, *58* (45), 16124−16129.

(31) Park, J.; Lee, Y.-M.; Nam, W.; Fukuzumi, S. Brønsted Acid-Promoted C−H Bond Cleavage via Electron Transfer from Toluene Derivatives to a Protonated Nonheme Iron(IV)-Oxo Complex with No Kinetic Isotope Effect. *J. Am. Chem. Soc.* **2013**, *135* (13), 5052−5061.

(32) Kim, S.; Cho, K.-B.; Lee, Y.-M.; Chen, J.; Fukuzumi, S.; Nam, W. Factors Controlling the Chemoselectivity in the Oxidation of Olefins by Nonheme Manganese(IV)-Oxo Complexes. *J. Am. Chem. Soc.* **2016**, *138* (33), 10654−10663.

(33) Jung, J.; Kim, S.; Lee, Y.-M.; Nam, W.; Fukuzumi, S. Switchover of the Mechanism between Electron Transfer and Hydrogen-Atom Transfer for a Protonated Manganese(IV)−Oxo Complex by Changing Only the Reaction Temperature. *Angew. Chem., Int. Ed.* **2016**, *55* (26), 7450−7454.

(34) Akiyama, T. Stronger Brønsted Acids. *Chem. Rev.* **2007**, *107* (12), 5744−5758.

(35) Park, J.; Morimoto, Y.; Lee, Y.-M.; Nam, W.; Fukuzumi, S. Proton-Promoted Oxygen Atom Transfer vs Proton-Coupled Electron Transfer of a Non-Heme Iron(IV)-Oxo Complex. *J. Am. Chem. Soc.* **2012**, *134* (8), 3903−3911.

(36) Lee, Y.-M.; Kim, S.; Ohkubo, K.; Kim, K.-H.; Nam, W.; Fukuzumi, S. Unified Mechanism of Oxygen Atom Transfer and Hydrogen Atom Transfer Reactions with a Triflic Acid-Bound Nonheme Manganese(IV)−Oxo Complex via Outer-Sphere Electron Transfer. *J. Am. Chem. Soc.* **2019**, *141* (6), 2614−2622.

(37) Miao, C.; Wang, B.; Wang, Y.; Xia, C.; Lee, Y.-M.; Nam, W.; Sun, W. Proton-Promoted and Anion-Enhanced Epoxidation of Olefins by Hydrogen Peroxide in the Presence of Nonheme Manganese Catalysts. *J. Am. Chem. Soc.* **2016**, *138* (3), 936−943.

(38) Huynh, M. H. V.; Meyer, T. J. Proton-Coupled Electron Transfer. *Chem. Rev.* **2007**, *107* (11), 5004−5064.

(39) Hammes-Schiffer, S. Theory of Proton-Coupled Electron Transfer in Energy Conversion Processes. *Acc. Chem. Res.* **2009**, *42* (12), 1881−1889.

(40) Weinberg, D. R.; Gagliardi, C. J.; Hull, J. F.; Murphy, C. F.; Kent, C. A.; Westlake, B. C.; Paul, A.; Ess, D. H.; McCafferty, D. G.; Meyer, T. J. Proton-Coupled Electron Transfer. *Chem. Rev.* **2012**, *112* (7), 4016−4093.

(41) Li, C.; Danovich, D.; Shaik, S. Blended Hydrogen Atom Abstraction and Proton-Coupled Electron Transfer Mechanisms of Closed-Shell Molecules. *Chem. Sci.* **2012**, *3* (6), 1903−1918.

(42) Devi, T.; Lee, Y.-M.; Nam, W.; Fukuzumi, S. Metal Ion-Coupled Electron-Transfer Reactions of Metal-Oxygen Complexes. *Coord. Chem. Rev.* **2020**, *410*, 213219.

(43) Josephy, T.; Kumar, R.; Bleher, K.; Röhs, F.; Glaser, T.; Rajaraman, G.; Comba, P. Synthesis, Characterization, and Reactivity of Bispidine-Iron(IV)-Tosylimido Species. *Inorg. Chem.* **2024**, *63*, 12109−12119.

(44) Zhang, J.; Wei, W.-J.; Lu, X.; Yang, H.; Chen, Z.; Liao, R.-Z.; Yin, G. Nonredox Metal Ions Promoted Olefin Epoxidation by Iron(II) Complexes with H2O2: DFT Calculations Reveal Multiple Channels for Oxygen Transfer. *Inorg. Chem.* **2017**, *56* (24), 15138−15149.

(45) Sun, D.; Wu, Z.; Zhang, X.; Yang, J.; Zhao, Y.; Nam, W.; Wang, Y. Brønsted Acids Promote Olefin Oxidations by Bioinspired Nonheme CoIII(PhIO)(OH) Complexes: A Role for Low-Barrier Hydrogen Bonds. *J. Am. Chem. Soc.* **2023**, *145* (10), 5739−5749.

(46) Wang, D.; Ray, K.; Collins, M. J.; Farquhar, E. R.; Frisch, J. R.; Gómez, L.; Jackson, T. A.; Kerscher, M.; Waleska, A.; Comba, P.; et al. Nonheme Oxoiron(Iv) Complexes of Pentadentate N5 Ligands: Spectroscopy, Electrochemistry, and Oxidative Reactivity. *Chem. Sci.* **2013**, *4* (1), 282−291.

(47) Singh, R.; Ganguly, G.; Malinkin, S. O.; Demeshko, S.; Meyer, F.; Nordlander, E.; Paine, T. K. A Mononuclear Nonheme Iron(IV)-Oxo Complex of a Substituted N4Py Ligand: Effect of Ligand Field on Oxygen Atom Transfer and C−H Bond Cleavage Reactivity. *Inorg. Chem.* **2019**, *58* (3), 1862−1876.

(48) Cho, K.-B.; Shaik, S.; Nam, W. Theoretical Investigations into C−H Bond Activation Reaction by Nonheme MnIVO Complexes: Multistate Reactivity with No Oxygen Rebound. *J. Phys. Chem. Lett.* **2012**, *3* (19), 2851−2856.

(49) Leto, D. F.; Massie, A. A.; Rice, D. B.; Jackson, T. A. Spectroscopic and Computational Investigations of a Mononuclear Manganese(IV)-Oxo Complex Reveal Electronic Structure Contributions to Reactivity. *J. Am. Chem. Soc.* **2016**, *138* (47), 15413−15424.

(50) Leto, D. F.; Ingram, R.; Day, V. W.; Jackson, T. A. Spectroscopic Properties and Reactivity of a Mononuclear Oxomanganese(Iv) Complex. *Chem. Commun.* **2013**, *49* (47), 5378−5380.

(51) Chen, J.; Cho, K.-B.; Lee, Y.-M.; Kwon, Y. H.; Nam, W. Mononuclear Nonheme Iron(Iv)−Oxo and Manganese(Iv)−Oxo Complexes in Oxidation Reactions: Experimental Results Prove Theoretical Prediction. *Chem. Commun.* **2015**, *51* (66), 13094−13097.

(52) Jung, J.; Kim, S.; Lee, Y.; Nam, W.; Fukuzumi, S. Switchover of the Mechanism between Electron Transfer and Hydrogen-Atom Transfer for a Protonated Manganese(IV)−Oxo Complex by Changing Only the Reaction Temperature. *Angew. Chem.* **2016**, *128* (26), 7576−7580.

(53) Shi, S.; Wang, Y.; Xu, A.; Wang, H.; Zhu, D.; Roy, S. B.; Jackson, T. A.; Busch, D. H.; Yin, G. Distinct Reactivity Differences of Metal Oxo and Its Corresponding Hydroxo Moieties in Oxidations: Implications from a Manganese(IV) Complex Having Dihydroxide Ligand. *Angew. Chem., Int. Ed.* **2011**, *50* (32), 7321−7324.

(54) Hull, J. F.; Balcells, D.; Sauer, E. L. O.; Raynaud, C.; Brudvig, G. W.; Crabtree, R. H.; Eisenstein, O. Manganese Catalysts for C−H Activation: An Experimental/Theoretical Study Identifies the Stereoelectronic Factor That Controls the Switch between Hydroxylation and Desaturation Pathways. *J. Am. Chem. Soc.* **2010**, *132* (22), 7605−7616.

(55) Frisch, M. J.; Trucks, G. W.; Schlegel, H. B.; Scuseria, G. E.; Robb, M. A.; Cheeseman, J. R.; Scalmani, G.; Barone, V.; Petersson, G. A.; Nakatsuji, H.; et al. Gaussian ∼ 16 {R}evision {B}.01. **2016**.

(56) Becke, A. D. Density-functional Thermochemistry. III. The Role of Exact Exchange. *J. Chem. Phys.* **1993**, *98* (7), 5648−5652.

(57) Becke, A. D. Density-Functional Exchange-Energy Approximation with Correct Asymptotic Behavior. *Phys. Rev. A* **1988**, *38*, 3098.

(58) Becke, A. D. Density-Functional Thermochemistry. V. Systematic Optimization of Exchange-Correlation Functionals. *J. Chem. Phys.* **1997**, *107* (20), 8554−8560.

(59) Sen, A.; Vyas, N.; Pandey, B.; Jaccob, M.; Rajaraman, G. Mechanistic Insights on the Formation of High-Valent MnIII/IV = O Species Using Oxygen as Oxidant: A Theoretical Perspective. *Isr. J. Chem.* **2020**, *60* (10−11), 973−986.

(60) Ansari, A.; Kaushik, A.; Rajaraman, G. Mechanistic Insights on the Ortho-Hydroxylation of Aromatic Compounds by Non-Heme Iron Complex: A Computational Case Study on the Comparative Oxidative Ability of Ferric-Hydroperoxo and High-Valent FeIV = O and FeV = O Intermediates. *J. Am. Chem. Soc.* **2013**, *135* (11), 4235−4249.

(61) Jaccob, M.; Ansari, A.; Pandey, B.; Rajaraman, G. Theoretical Studies on Concerted versus Two Steps Hydrogen Atom Transfer Reaction by Non-Heme MnIV/III=O Complexes: How Important Is the Oxo Ligand Basicity in the C−H Activation Step? *Dalton Trans.* **2013**, *42* (47), 16518−16526.

(62) Sun, X.; Geng, C.; Huo, R.; Ryde, U.; Bu, Y.; Li, J. Large Equatorial Ligand Effects on C−H Bond Activation by Nonheme Iron(IV)-Oxo Complexes. *J. Phys. Chem. B* **2014**, *118* (6), 1493−1500.

(63) Quesne, M. G.; Senthilnathan, D.; Singh, D.; Kumar, D.; Maldivi, P.; Sorokin, A. B.; de Visser, S. P. Origin of the Enhanced Reactivity of μ-Nitrido-Bridged Diiron(IV)-Oxo Porphyrinoid Complexes over Cytochrome P450 Compound I. *ACS Catal.* **2016**, *6* (4), 2230−2243.

(64) Siegbahn, P. E. M.; Borowski, T. Modeling Enzymatic Reactions Involving Transition Metals. *Acc. Chem. Res.* **2006**, *39* (10), 729−738.

(65) Grimme, S.; Ehrlich, S.; Goerigk, L. Effect of the Damping Function in Dispersion Corrected Density Functional Theory. *J. Comput. Chem.* **2011**, *32* (7), 1456−1465.

(66) Grimme, S.; Antony, J.; Ehrlich, S.; Krieg, H. A Consistent and Accurate Ab Initio Parametrization of Density Functional Dispersion Correction (DFT-D) for the 94 Elements H-Pu. *J. Chem. Phys.* **2010**, *132*, 154104.

(67) Hehre, W. J.; Ditchfield, R.; Pople, J. A. Self—Consistent Molecular Orbital Methods. XII. Further Extensions of Gaussian—Type Basis Sets for Use in Molecular Orbital Studies of Organic Molecules. *J. Chem. Phys.* **1972**, *56* (5), 2257−2261.

(68) Fuentealba, P.; Preuss, H.; Stoll, H.; Von Szentpály, L. A Proper Account of Core-Polarization with Pseudopotentials: Single Valence-Electron Alkali Compounds. *Chem. Phys. Lett.* **1982**, *89* (5), 418−422.

(69) Weigend, F.; Ahlrichs, R. Balanced Basis Sets of Split Valence{,} Triple Zeta Valence and Quadruple Zeta Valence Quality for H to Rn: Design and Assessment of Accuracy. *Phys. Chem. Chem. Phys.* **2005**, *7* (18), 3297−3305.

(70) Weigend, F. Accurate Coulomb-Fitting Basis Sets for H to Rn. *Phys. Chem. Chem. Phys.* **2006**, *8* (9), 1057−1065.

(71) Tomasi, J.; Mennucci, B.; Cammi, R. Quantum Mechanical Continuum Solvation Models. *Chem. Rev.* **2005**, *105* (8), 2999−3094.

(72) Britto, N. J.; Sen, A.; Rajaraman, G. Unravelling the Effect of Acid-Driven Electron Transfer in High-Valent FeIV = O/MnIV = O Species and Its Implications for Reactivity. *Chem. Asian J.* **2023**, *18* (23), 1−10.

(73) Neese, F. Software Update: The ORCA Program System—Version 5.0. *Wiley Interdiscip. Rev.: Comput. Mol. Sci.* **2022**, *12* (5), No. e1606.

(74) Gaggioli, C. A.; Stoneburner, S. J.; Cramer, C. J.; Gagliardi, L. Beyond Density Functional Theory: The Multiconfigurational Approach To Model Heterogeneous Catalysis. *ACS Catal.* **2019**, *9* (9), 8481−8502.

(75) Cho, K.-B.; Shaik, S.; Nam, W. Theoretical Investigations into C−H Bond Activation Reaction by Nonheme MnIVO Complexes: Multistate Reactivity with No Oxygen Rebound. *J. Phys. Chem. Lett.* **2012**, *3*, 2851−2856.

(76) Rice, D. B.; Massie, A. A.; Jackson, T. A. Experimental and Multireference ab Initio Investigations of Hydrogen-Atom-Transfer Reactivity of a Mononuclear MnIV-oxo Complex. *Inorg. Chem.* **2019**, *58*, 13902−13916.

(77) Singh, P.; Massie, A. A.; Denler, M. C.; Lee, Y.; Mayfield, J. R.; Lomax, M. J. A.; Singh, R.; Nordlander, E.; Jackson, T. A. C−H Bond Oxidation by MnIV−Oxo Complexes: Hydrogen-Atom Tunneling and Multistate Reactivity. *Inorg. Chem.* **2024**, *63*, 7754−7769.

(78) Sen, A.; Ansari, A.; Swain, A.; Pandey, B.; Rajaraman, G. Probing the Origins of Puzzling Reactivity in Fe/Mn−Oxo/Hydroxo Species toward C−H Bonds: A DFT and Ab Initio Perspective. *Inorg. Chem.* **2023**, *62*, 14931−14941.

(79) Martin, F.; Zipse, H. Charge Distribution in the Water Molecule—A Comparison of Methods. *J. Comput. Chem.* **2005**, *26* (1), 97−105.

(80) Biegler-König, F.; Schönbohm, J. Update of the AIM2000-Program for Atoms in Molecules. *J. Comput. Chem.* **2002**, *23* (15), 1489−1494.

(81) Lu, T.; Chen, F. Multiwfn: A Multifunctional Wavefunction Analyzer. *J. Comput. Chem.* **2012**, *33* (5), 580−592.

(82) Stuyver, T.; Huang, J.; Mallick, D.; Danovich, D.; Shaik, S. TITAN: A Code for Modeling and Generating Electric Fields—Features and Applications to Enzymatic Reactivity. *J. Comput. Chem.* **2020**, *41* (1), 74−82.

(83) Leto, D. F.; Massie, A. A.; Rice, D. B.; Jackson, T. A. Spectroscopic and Computational Investigations of a Mononuclear Manganese(IV)-Oxo Complex Reveal Electronic Structure Contributions to Reactivity. *J. Am. Chem. Soc.* **2016**, *138*, 15413−15424.

(84) Sen, A.; Kumar, R.; Rajaraman, G. A Theoretical Perspective on the Reactivity of High-Valent Mn-Oxo/Nitrene Species towards Oxidative Transformations. *Inorg. Chim. Acta* **2022**, *529* (2021), 120654.

(85) Puri, M.; Que, L. Toward the Synthesis of More Reactive S = 2 Non-Heme Oxoiron(IV) Complexes. *Acc. Chem. Res.* **2015**, *48* (8), 2443−2452.

(86) Hirao, H.; Kumar, D.; Que, L. J.; Shaik, S. Two-State Reactivity in Alkane Hydroxylation by Non-Heme Iron−Oxo Complexes. *J. Am. Chem. Soc.* **2006**, *128* (26), 8590−8606.

(87) Lee, Y. M.; Kim, S.; Ohkubo, K.; Kim, K. H.; Nam, W.; Fukuzumi, S. Unified Mechanism of Oxygen Atom Transfer and Hydrogen Atom Transfer Reactions with a Triflic Acid-Bound Nonheme Manganese(IV)-Oxo Complex via Outer-Sphere Electron Transfer. *J. Am. Chem. Soc.* **2019**, *141* (6), 2614−2622.

(88) Sharma, N.; Lee, Y.-M.; Li, X.-X.; Nam, W.; Fukuzumi, S. Singly Unified Driving Force Dependence of Outer-Sphere Electron-Transfer Pathways of Nonheme Manganese(IV)−Oxo Complexes in the Absence and Presence of Lewis Acids. *Inorg. Chem.* **2019**, *58* (20), 13761−13765.

(89) Nam, P.-C.; Nguyen, M. T.; Chandra, A. K. The C−H and α(C−X) Bond Dissociation Enthalpies of Toluene, C6H5-CH2X (X = F, Cl), and Their Substituted Derivatives: A DFT Study. *J. Phys. Chem. A* **2005**, *109* (45), 10342−10347.

(90) Steen, J. D.; Stepanovic, S.; Parvizian, M.; de Boer, J. W.; Hage, R.; Chen, J.; Swart, M.; Gruden, M.; Browne, W. R. Lewis versus Brønsted Acid Activation of a Mn(IV) Catalyst for Alkene Oxidation. *Inorg. Chem.* **2019**, *58*, 14924−14930.

(91) Stuyver, T.; Ramanan, R.; Mallick, D.; Shaik, S. Oriented (Local) Electric Fields Drive the Millionfold Enhancement of the H-Abstraction Catalysis Observed for Synthetic Metalloenzyme Analogues. *Angew. Chem., Int. Ed.* **2020**, *59* (20), 7915−7920.